

# Early Lunar Magnetism

Ian Garrick-Bethell,<sup>1\*</sup> Benjamin P. Weiss,<sup>1</sup> David L. Shuster,<sup>2</sup> Jennifer Buz<sup>1</sup>

It is uncertain whether the Moon ever formed a metallic core or generated a core dynamo. The lunar crust and returned samples are magnetized, but the source of this magnetization could be meteoroid impacts rather than a dynamo. Here, we report magnetic measurements and <sup>40</sup>Ar/<sup>39</sup>Ar thermochronological calculations for the oldest known unshocked lunar rock, troctolite 76535. These data imply that there was a long-lived field on the Moon of at least 1 microtesla ~4.2 billion years ago. The early age, substantial intensity, and long lifetime of this field support the hypothesis of an ancient lunar core dynamo.

**B**efore the Apollo missions, the Moon was often thought to be a primordial undifferentiated relic of the early solar system (1) that had never formed a core or generated a magnetic dynamo. Because it was well known that the Moon presently has no global magnetic field (2), it was a surprise when the Apollo subsatellites and surface magnetometers detected magnetic fields originating from the lunar crust (3), and paleo-

magnetic analyses of returned samples identified natural remanent magnetization (NRM) (4). The magnetization of many samples must have been produced by ancient magnetic fields, but the association of crustal magnetization with impact structures (5, 6) and the identification of NRM in <200-million-year-old impact glasses (7) suggest that the field sources could have been impact-generated plasmas (8–11) rather than a core dynamo

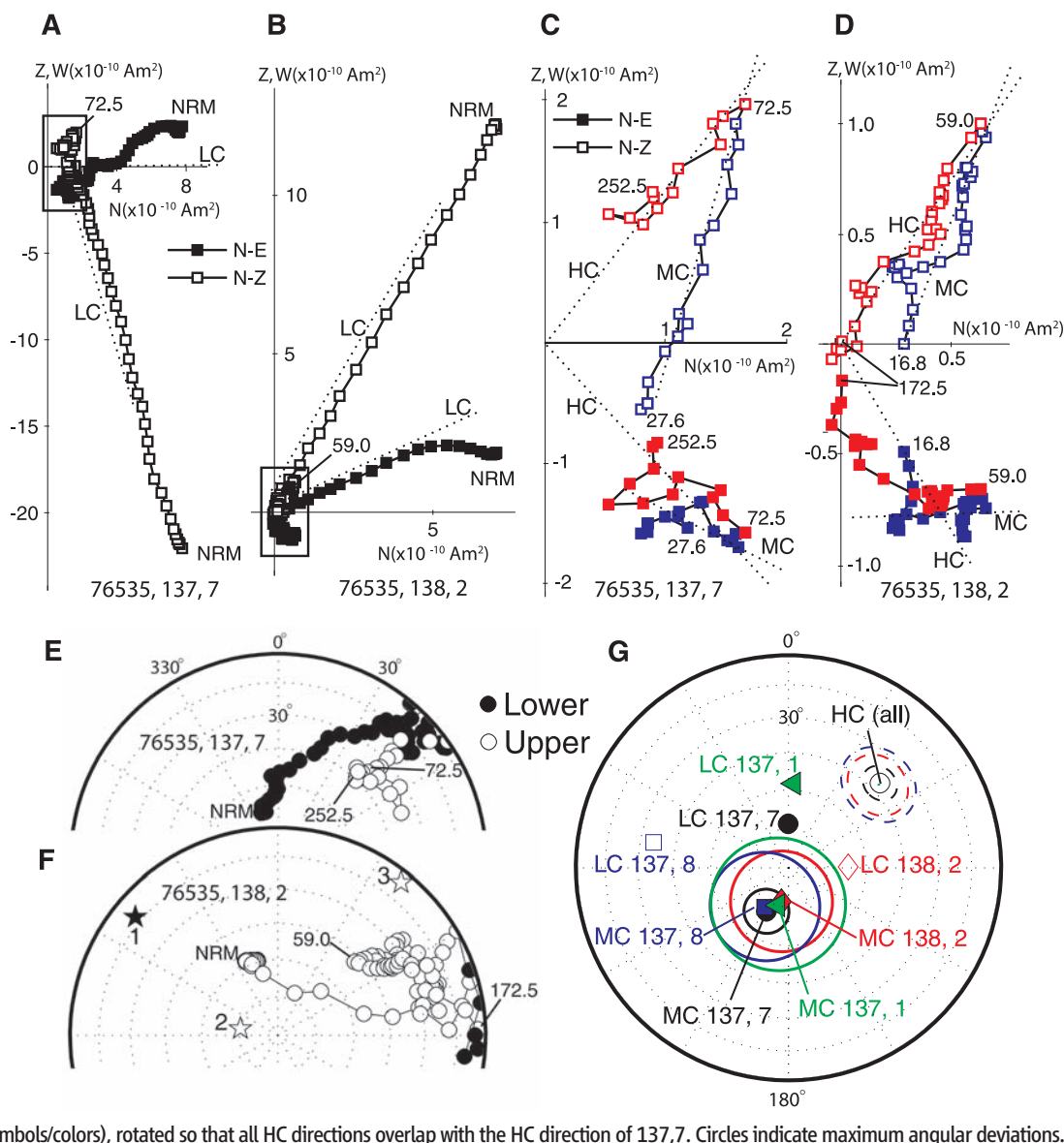
(12). Determining the source of lunar paleofields is critical for understanding the thermal evolution of the Moon, the limits of dynamo generation in small bodies, and, by implication, the magnetization of asteroids and meteorites.

A key difficulty is that available lunar rocks are often poor recorders of magnetic fields (13, 14). Most highlands samples are brecciated and/or shocked, making it difficult to distinguish between NRM acquired instantaneously during shock-magnetization or from long-lived dynamo fields (11). A further complication is that the precise thermal histories of most lunar rocks are unknown. Their magnetization ages have often been assumed to be equal to their radiometric ages (14), even

<sup>1</sup>Department of Earth, Atmospheric, and Planetary Sciences, Massachusetts Institute of Technology, 54-521, 77 Massachusetts Avenue, Cambridge, MA 02139, USA. <sup>2</sup>Berkeley Geochronology Center, 2455 Ridge Road, Berkeley, CA 94709, USA.

\*To whom correspondence should be addressed. E-mail: iang@mit.edu

**Fig. 1.** NRM in troctolite 76535. (A to D) Two-dimensional projection of the NRM vector during AF demagnetization. Closed symbols represent end points of magnetization projected onto the horizontal N and E planes, and open symbols represent end points of magnetization projected onto the vertical N and Z planes. Peak fields for selected AF steps are labeled in mT. Dashed lines are component directions determined from principal component analyses (PCA). (A) AF demagnetization of 76535,137,7 up to 252.5 mT and its LC component. (B) AF demagnetization of 76535,138,2 up to 172.5 mT and its LC component. (C) Zoom of boxed region in (A), showing data for the MC (blue) and HC (red) components. Data points are from averages of a total of 185 AF measurements. The HC direction is anchored to the origin. (D) Zoom of boxed region in (B), showing data for the MC (blue) and HC (red) components. Data points are from averages of a total of 1450 AF measurements. The HC direction is anchored to the origin. (E) Equal-area projection of the remanence directions shown in (A). (F) Equal-area projection of the remanence directions shown in (B) and first, second, and third principal axes of the anisotropy of remanence ellipsoid (stars), calculated with a 100-μT bias field ARM in a peak AF field of 57 mT. (G) LC, MC, and HC components obtained from PCA of four subsamples studied (four symbols/colors), rotated so that all HC directions overlap with the HC direction of 137,7. Circles indicate maximum angular deviations.



though thermal events that can remagnetize rocks may have no effect on most geochronometers.

Here, we report a magnetic study of an unshocked ancient rock with a well-constrained thermal history, troctolite 76535. We applied  $^{40}\text{Ar}/^{39}\text{Ar}$  thermochronological constraints (15) in conjunction with paleomagnetism to determine when 76535 was last remagnetized and to constrain the nature and duration of the recorded paleofields. Because of the putative late heavy bombardment at ~3.9 billion years ago (Ga), there are few lunar rocks with  $^{40}\text{Ar}/^{39}\text{Ar}$  ages older than ~4.0 billion years and no paleomagnetic analyses from before this time. However, it is during this early epoch when a convecting core dynamo is most thermally plausible (16). 76535 is the only known unshocked (17–19) whole rock from this epoch (20).

76535 was found in a rake sample from the ejecta blanket of a 10-m-diameter impact crater (21). Four different chronometers (U/Pb, Th/Pb, Sm/Nd, and  $^{40}\text{Ar}/^{39}\text{Ar}$ ) yielded indistinguishable ages of 4.2 to 4.3 billion years (22–26). Its Rb/Sr age is less certain because of spurious effects associated with olivine separates, ranging between 4.61 to 4.38 Ga (24, 27). The rock contains the ferromagnetic Fe-Ni-Co minerals kamacite and taenite as free grains and as inclusions of oriented linear arrays and needles (with axial ratios up to 45:1) in plagioclase (17–19). An unsuccessful Thellier-Thellier paleointensity experiment on 76535 (14) indicated that it contains a highly stable NRM composed of at least two components and that its Curie point is >780°C. The Co content of its iron metal, up to 6 weight percent, among the largest measured for any lunar sample (17, 28), would indicate a Curie point of ~850°C (29).

To determine if 76535 has a record of lunar magnetic paleofields, we conducted nondestructive alternating field (AF) demagnetization of six unoriented polycrystalline chips. AF data for our four most carefully controlled samples (137,1; 137,7;

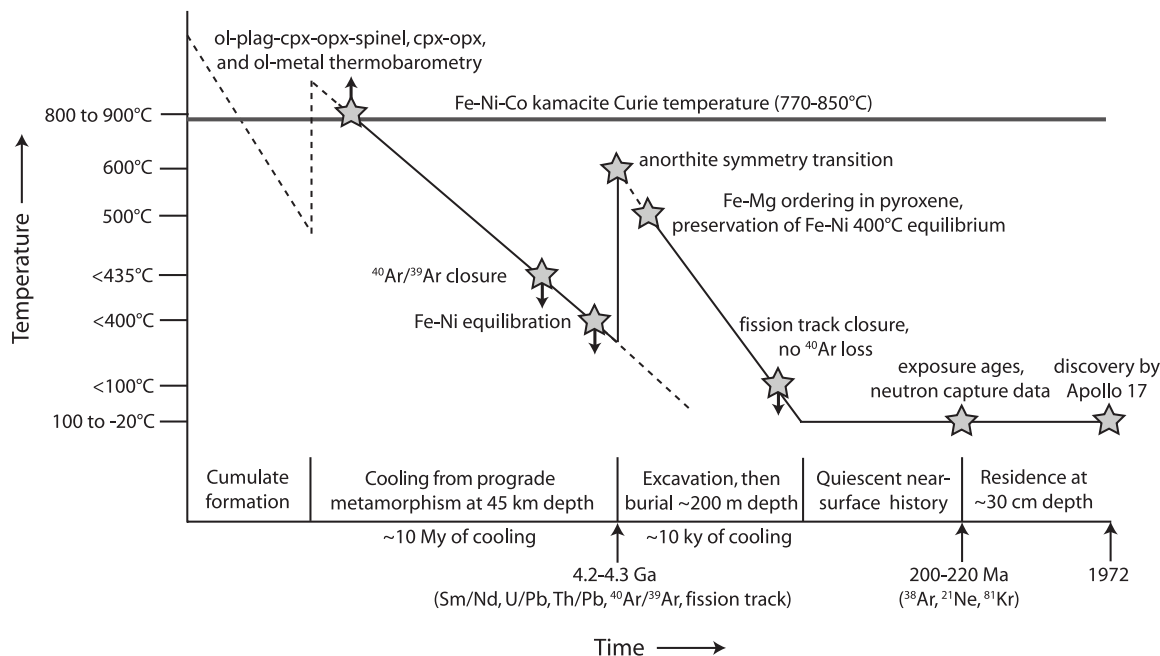
137,8; and 138,2) demonstrate that the NRM consists of low coercivity (LC), medium coercivity (MC), and hard coercivity (HC) components [supporting online material (SOM) text]. The LC component, blocked below ~12 mT, is apparently a combination of viscous remanent magnetization and an isothermal remanent magnetization (IRM) with a non-unidirectional orientation relative to the MC and HC components (Fig. 1, A and B, and figs. S1 and S2), resembling that observed in many other Apollo samples (14, 30) and meteorites (31). The MC component is much weaker than the LC component and extends from ~15 mT to between 45 and 83 mT (Fig. 1, C and D, and figs. S1 and S2, blue). A final HC component trends to the origin from 45 to between 83 and >250 mT, suggesting that it is the final primary component (Fig. 1, C and D, and figs. S1 and S2, red). The angular distances between the MC and HC components for all four subsamples after correction for anisotropy of remanence are similar (142° to 149°) and are consistent with the two components being unidirectional across the 76535 parent rock (Fig. 1G). The high coercivities of NRM are also consistent with the pseudo-single-domain state of the iron in plagioclase-rich subsamples (fig. S11). The inferred paleointensities (SOM text) for the MC and HC components obtained using the anhysteretic remanent magnetization (ARM) and IRM methods are at least 0.3 to 1  $\mu\text{T}$  and possibly an order of magnitude larger (for comparison, the intensity of Earth's dynamo field at the Earth's surface is ~50  $\mu\text{T}$ ). Such paleointensities are far larger than that expected from external sources like the Earth, sun, protoplanetary disk, or galaxy from 4.3 to 4.2 Ga (SOM text) but are consistent with fields generated by meteoroid impacts and a lunar core dynamo.

The latter two possibilities can be distinguished by use of a diversity of petrologic and geochronologic data on 76535. The complete lack

of shock features in 76535 [peak shock pressures of <5 GPa (17)] argues against isothermal shock remanent magnetization (SRM) [which for these pressures typically blocks below coercivities of <~30 mT (32, 33)], as well as the possibility of shock-produced thermoremanent magnetization (TRM) [the temperature increase for any shock of <5 GPa is negligible (34, 35)]. The low ratio of NRM to saturation IRM above 15 mT rules out magnetization by impact-generated (36) and artificial IRM fields. These data indicate that nonshock TRM is the most likely explanation for the MC component and much of the HC component (37).

Petrologic analyses suggest that 76535 experienced only two cooling events that could have blocked TRM (Fig. 2). The rock crystallized as a cumulate at ~45 km depth (17, 18, 38), and multiple thermobarometers indicate that it later experienced prograde metamorphism to peak temperatures of >800° to 900°C (38–42). The observed equilibrium compositions of kamacite and taenite indicate that it then cooled slowly (at ~10°C per million years) to at least ~400°C (17), over which time five independent geochronometers closed to yield radiometric ages that are indistinguishable within their uncertainties of 50 to 100 million years ago (Ma). Observations of Fe-Mg ordering in 76535 orthopyroxene indicate that after excavation, it was heated again to at least 500°C and then cooled more rapidly to ~20°C (the lunar near-surface temperature) over a period of ~10,000 years, probably in an ejecta blanket at ~200 m depth (39). Extrapolation of measurements of the diffusivity of Ni in taenite (43, 44) and the observation that the 400°C kamacite equilibrium composition was preserved after excavation imply that the peak temperature reached during burial was <500° to 600°C. This prediction is also in agreement with the 600°C temperature inferred from symmetry transitions in 76535 anorthite that formed during rapid cooling

**Fig. 2.** Thermal history of troctolite 76535, as inferred from a variety of petrologic and geochronometric measurements. Stars and solid lines indicate relatively well-constrained times and temperatures. Dashed lines indicate less-certain time-temperature histories. References for the various data sets described here are found in the main text. Axes are not linearly scaled. My, million years; ky, thousand years.



(19, 45). A final event excavated the rock to a depth of ~30 cm where it remained for much of the last ~220 million years (23).

Fission track data (46), in conjunction with our calculations using  $^{40}\text{Ar}/^{39}\text{Ar}$  data (25), demonstrate that initial excavation took place at ~4.2 Ga. Because the rock was heated to 500° to 600°C after initial excavation, its fission track age (~4.2 billion years, when corrected for annealing at ambient lunar surface temperatures) must have been completely reset at this time [see (47, 48)]. The lack of evidence for Ar loss after 4.2 Ga places a conservative upper bound of heating for ~50 years at 500°C at 3.9 Ga, the time of major basin formation, or several hours at 800°C (Fig. 3) (SOM text). Limits placed on events since 3.9 Ga are even more stringent (Fig. 3C). Therefore, a simple interpretation of these magnetic data are that the HC component was acquired during slow cooling in the deep crust at ~4.2 Ga and the MC component was acquired just after excavation during cooling in an ejecta blanket over ~10,000 years. The cooling rates experienced by 76535 during both events require that the magnetizing fields persisted for far longer than expected for the

longest-lived impact-generated fields [just ~1 day for the largest basins (10)]. The slow cooling rate for the HC component indicates that the field was stable over millions of years, comparable to superchrons on Earth during the last several hundred million years (49).

Although the Ar data are permissive of extremely brief ad hoc heating events (such as those from deposition in shallow ejecta blankets) after 4.2 Ga, we can demonstrate that even if such events took place, the durations of the magnetic fields from such impacts are too short to be a plausible source of the magnetization in 76535. Conductive heating from a hot ejecta blanket would raise the temperature of the ~5-cm-diameter rock (conservatively assuming it has always been no larger than its size as sampled by Apollo 17) from ~20°C (ambient subsurface) to 770°C (the minimum Curie temperature) in approximately 1000 s (fig. S12). However, spontaneously generated fields due to plasma currents or motion of charged ejecta are believed to disappear in  $<10^2$  s for craters <100 km in diameter (8, 9), before the rock could even begin to cool and acquire TRM. Such short thermal events are also unlikely to have occurred

during the last 4 billion years because they would require the rock to be in a thin ejecta blanket unrealistically close to the surface (<10 cm) (fig. S12), in contradiction with its exposure age of 220 million years and neutron capture data (23, 50). Even the day-long impact-generated fields that may have been present during major basin formation ~3.9 Ga would require an unrealistically small <~1-m-thick ejecta blanket to permit 76535 to acquire TRM (SOM text). Therefore, the most reasonable remaining origin for the high-coercivity NRM in 76535 is from long-lived magnetic fields like those expected from a core dynamo.

The plausibility of a lunar dynamo has been questioned because of the unconfirmed existence of a fluid metallic core (51), the difficulty of sustaining a dynamo at least 600 million years after accretion (16, 52), and large paleointensities of ~100  $\mu\text{T}$  that are difficult to reconcile with theoretical predictions (51, 53). However, recent predictions of the effect of dissipation at a liquid-core mantle boundary on the orientation of the lunar spin axis (54) and refined measurements of the tidal Love number (55) have provided growing evidence that the Moon even today has a small

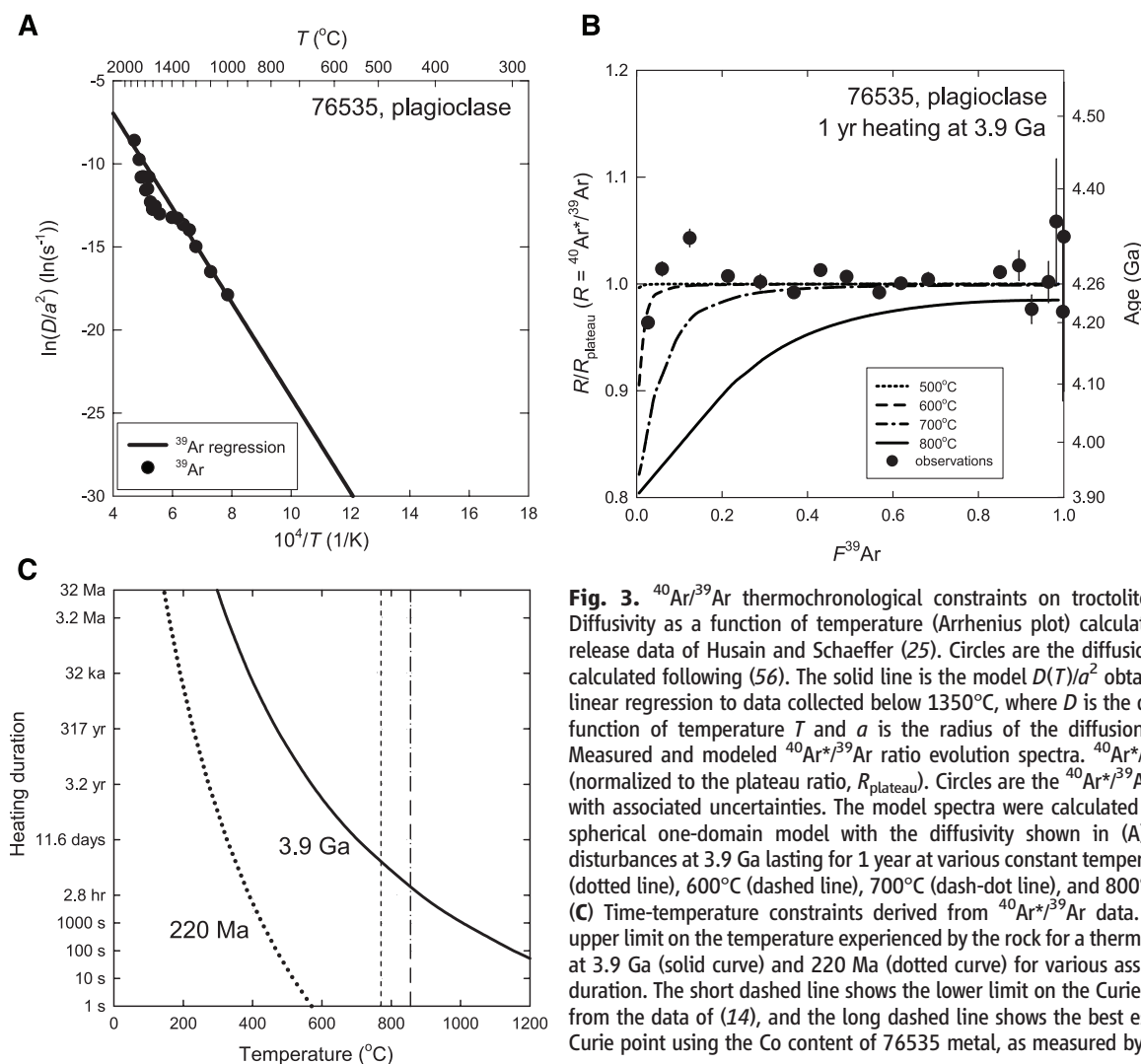


**Fig. 3.**  $^{40}\text{Ar}/^{39}\text{Ar}$  thermochronological constraints on troctolite 76535. **(A)** Diffusivity as a function of temperature (Arrhenius plot) calculated from  $^{39}\text{Ar}$  release data of Husain and Schaeffer (25). Circles are the diffusion coefficients calculated following (56). The solid line is the model  $D(T)/a^2$  obtained from the linear regression to data collected below 1350°C, where  $D$  is the diffusivity as a function of temperature  $T$  and  $a$  is the radius of the diffusion domain. **(B)** Measured and modeled  $^{40}\text{Ar}/^{39}\text{Ar}$  ratio evolution spectra.  $^{40}\text{Ar}/^{39}\text{Ar}$  ratios,  $R$  (normalized to the plateau ratio,  $R_{\text{plateau}}$ ). Circles are the  $^{40}\text{Ar}/^{39}\text{Ar}$  data of (25) with associated uncertainties. The model spectra were calculated with use of a spherical one-domain model with the diffusivity shown in (A) for thermal disturbances at 3.9 Ga lasting for 1 year at various constant temperatures: 500°C (dotted line), 600°C (dashed line), 700°C (dash-dot line), and 800°C (solid line). **(C)** Time-temperature constraints derived from  $^{40}\text{Ar}/^{39}\text{Ar}$  data. Shown is an upper limit on the temperature experienced by the rock for a thermal disturbance at 3.9 Ga (solid curve) and 220 Ma (dotted curve) for various assumed heating duration. The short dashed line shows the lower limit on the Curie point derived from the data of (14), and the long dashed line shows the best estimate of the Curie point using the Co content of 76535 metal, as measured by (17).



(~350-km radius) partially liquid core. Furthermore, the field that magnetized 76535, which is ~300 million years older than that recorded by all previously studied lunar samples, is from the early epoch when the Moon would have most likely had a convecting core due to enhanced heat flow and a possible cumulate overturn event (52). Finally, the NRM in 76535 indicates that minimum paleointensities were of order microteslas, consistent with the theoretical expectations for a lunar core dynamo (53). Our data and these considerations suggest that at 4.2 Ga, the Moon possessed a dynamo field, and by implication a convecting metallic core.

## References and Notes

- H. C. Urey, *Geochim. Cosmochim. Acta* **1**, 209 (1951).
- N. F. Ness, K. W. Behannon, C. S. Searce, S. C. Cantarano, *J. Geophys. Res.* **72**, 5769 (1967).
- P. Dyal, C. W. Packer, C. P. Sonett, *Science* **169**, 762 (1970).
- S. K. Runcorn *et al.*, *Science* **167**, 697 (1970).
- J. S. Halekas, R. P. Lin, D. L. Mitchell, *Meteorit. Planet. Sci.* **38**, 565 (2003).
- D. L. Mitchell *et al.*, *Icarus* **194**, 401 (2008).
- N. Sugiura, Y. M. Wu, D. W. Strangway, G. W. Pearce, L. A. Taylor, *Proc. Lunar Planet. Sci. Conf.* **10**, 2189 (1979).
- L. J. Srnka, *Proc. Lunar Sci. Conf.* **8**, 785 (1977).
- D. A. Crawford, P. H. Schultz, *Int. J. Impact Eng.* **23**, 169 (1999).
- L. L. Hood, N. A. Artemieva, *Icarus* **193**, 485 (2008).
- R. R. Doell, C. S. Gromme, A. N. Thorpe, F. E. Senftle, *Science* **167**, 695 (1970).
- S. K. Runcorn, *Nature* **275**, 430 (1978).
- M. Fuller, S. M. Cisowski, in *Geomagnetism*, vol. 2, J. A. Jacobs, Ed. (Academic Press, New York, 1987), pp. 307–456.
- K. P. Lawrence, C. L. Johnson, L. Tauxe, J. Gee, *Phys. Earth Planet. Int.* **10.1016/j.pepi.2008.05.007** (2008).
- D. L. Shuster, B. P. Weiss, *Science* **309**, 594 (2005).
- D. J. Stevenson, *Rep. Prog. Phys.* **46**, 555 (1983).
- R. Gooley, R. Brett, J. R. Smyth, J. Warner, *Geochim. Cosmochim. Acta* **38**, 1329 (1974).
- R. F. Dymek, A. L. Albee, A. A. Chodos, *Proc. Lunar Sci. Conf.* **6**, 301 (1975).
- G. L. Nord, *Proc. Lunar Sci. Conf.* **7**, 1875 (1976).
- D. E. Wilhelms, "The Geologic History of the Moon" [Professional Paper 1348, U.S. Geological Survey (USGS), Government Printing Office, Washington, DC, 1987].
- E. W. Wolfe, "The Geologic Investigation of the Taurus-Littrow Valley: Apollo 17 Landing Site" (Professional Paper 1080, Government Printing Office, Washington, DC, 1981).
- J. C. Huneke, G. J. Wasserburg, *Lunar Sci.* **VI**, 417 (1975).
- G. W. Lugmair, K. Marti, J. P. Kurtz, N. B. Scheinin, *Proc. Lunar Sci. Conf.* **7**, 2009 (1976).
- W. R. Premo, M. Tatsumoto, *Proc. Lunar Planet. Sci. Conf.* **22**, 381 (1992).
- L. Husain, O. A. Schaeffer, *Geophys. Res. Lett.* **2**, 29 (1975).
- D. D. Bogard, L. E. Nyquist, B. M. Bansal, H. Wiesmann, C.-Y. Shih, *Earth Planet. Sci. Lett.* **26**, 69 (1975).
- D. A. Papanastassiou, G. J. Wasserburg, *Proc. Lunar Sci. Conf.* **7**, 2035 (1976).
- G. Ryder, M. D. Norman, R. A. Score, *Proc. Lunar Planet. Sci. Conf.* **11**, 471 (1980).
- R. M. Bozorth, *Ferromagnetism*. (IEEE Press, New York, 1951), pp. 968.
- G. W. Pearce, D. W. Strangway, "Apollo 16: Preliminary Science Report" (SP-315, NASA, 1972), chap. 7C, pp. 7–55.
- J. Gattacceca, P. Rochette, *Earth Planet. Sci. Lett.* **227**, 377 (2004).
- J. Gattacceca *et al.*, *Phys. Earth Planet. Inter.* **166**, 1 (2008).
- J. Pohl, A. Eckstaller, *Lunar Planet. Sci.* **12**, 851 (1981).
- A. Bischoff, D. Stoffer, *Eur. J. Mineral.* **4**, 707 (1992).
- N. Artemieva, B. Ivanov, *Icarus* **171**, 84 (2004).
- L. Carporzen, S. A. Gilder, R. J. Hart, *Nature* **435**, 198 (2005).
- Because some kamacite would have exsolved from taenite during slow-cooling in the deep lunar crust, the HC component is probably a mixture of nonshock TRM and phase-transformation crystallization remanent magnetization (SOM text).
- I. S. McCallum, J. M. Schwartz, *J. Geophys. Res.* **106**, 27969 (2001).
- I. S. McCallum *et al.*, *Geochim. Cosmochim. Acta* **70**, 6068 (2006).
- D. H. Lindsay, D. J. Andersen, *Proc. Lunar Planet. Sci. Conf.* **13**, A887 (1983).
- C. T. Herzberg, *Lunar Planet. Sci.* **10**, 537 (1979).
- R. H. Hewins, J. I. Goldstein, *Lunar Planet. Sci.* **6**, 356 (1975).
- K. Richter, A. J. Campbell, M. Humayun, *Geochim. Cosmochim. Acta* **69**, 3145 (2005).
- A. Meibom *et al.*, *Science* **288**, 839 (2000).
- J. R. Smyth, *Proc. Lunar Planet. Sci. Conf.* **17**, E91 (1986).
- D. Braddy, I. D. Hutcheon, P. B. Price, *Proc. Lunar Sci. Conf.* **6**, 3587 (1975).
- C. W. Naeser, H. Faul, *J. Geophys. Res.* **74**, 705 (1969).
- R. A. Ketcham, R. A. Donelick, W. D. Carlson, *Am. Mineral.* **84**, 1235 (1999).
- R. B. Merrill, M. W. M. McElhinny, *The Magnetic Field of the Earth: Paleomagnetism, the Core, and the Deep Mantle* (Academic Press, San Diego, 1998), p. 531.
- It is plausible that a small (<10 cm), highly localized, magmatic dike could heat a sample for short timescales; however, such an event would be highly fortuitous, and even more fortuitous to have taken place simultaneously with an impact event.
- D. W. Collinson, *Surv. Geophys.* **14**, 89 (1993).
- D. R. Stegman, M. A. Jellinek, S. A. Zatman, J. R. Baumgardner, M. A. Richards, *Nature* **421**, 143 (2003).
- M. A. Wieczorek *et al.*, *Rev. Mineral. Geochem.* **60**, 221 (2006).
- J. R. Williams, D. H. Boggs, C. F. Yoder, J. T. Ratcliff, *J. Geophys. Res.* **106**, 27933 (2001).
- S. Goossens, K. Matsumoto, *Geophys. Res. Lett.* **35**, L02204 (2008).
- H. Fechtig, S. T. Kalbitzer, in *Potassium Argon Dating*, O. A. Schaeffer, J. Zahringer, Eds. (Springer-Verlag, New York, 1966), pp. 68–107.
- We thank the Johnson Space Center staff and the Curation and Analysis Planning Team for Extraterrestrial Materials for allocating 76535; V. Fernandes for insights into lunar  $^{40}\text{Ar}/^{39}\text{Ar}$  geochronology; I. S. McCallum for discussions about thermobarometry; S. Slotznick and S. Pedersen for help with the paleomagnetic analyses; M. Zuber and T. Bosak for suggestions; and K. Willis for administrative help. B.P.W., D.L.S., and I.G.-B. thank the NASA Lunar Advanced Science and Exploration Research Program; B.P.W. thanks the Charles E. Reed Faculty Initiatives Fund for support; and D.L.S. thanks the Ann and Gordon Getty Foundation.

## Supporting Online Material

www.sciencemag.org/cgi/content/full/323/5912/356/DC1  
SOM Text  
Figures S1 to S12  
Tables S1 to S3  
References

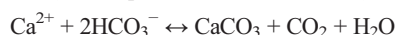
6 October 2008; accepted 3 December 2008  
10.1126/science.1166804

# Contribution of Fish to the Marine Inorganic Carbon Cycle

R. W. Wilson,<sup>1\*</sup> F. J. Millero,<sup>2\*</sup> J. R. Taylor,<sup>2</sup> P. J. Walsh,<sup>2,3</sup> V. Christensen,<sup>4</sup> S. Jennings,<sup>5</sup> M. Grosell<sup>2\*</sup>

Oceanic production of calcium carbonate is conventionally attributed to marine plankton (coccolithophores and foraminifera). Here we report that marine fish produce precipitated carbonates within their intestines and excrete these at high rates. When combined with estimates of global fish biomass, this suggests that marine fish contribute 3 to 15% of total oceanic carbonate production. Fish carbonates have a higher magnesium content and solubility than traditional sources, yielding faster dissolution with depth. This may explain up to a quarter of the increase in titratable alkalinity within 1000 meters of the ocean surface, a controversial phenomenon that has puzzled oceanographers for decades. We also predict that fish carbonate production may rise in response to future environmental changes in carbon dioxide, and thus become an increasingly important component of the inorganic carbon cycle.

The inorganic half of the marine carbon cycle includes biogenic reaction of seawater calcium ( $\text{Ca}^{2+}$ ) with bicarbonate ( $\text{HCO}_3^-$ ), producing insoluble calcium carbonate ( $\text{CaCO}_3$ ) in the process of calcification (1):



The vast majority of oceanic calcification is by planktonic organisms (2). Coccolithophores are considered to be the major contributor, but foraminifera are also included in global carbonate budgets (3). Upon death, their carbonate "skeletons" are released and rapidly sink to deeper ocean layers. Based on observations and models, estimates of global production of new  $\text{CaCO}_3$

range from 0.7 to 1.4 Pg  $\text{CaCO}_3\text{-C year}^{-1}$  (4–7) (Fig. 1).

It is less widely known that all marine teleosts (bony fish) produce and excrete carbonate pre-

<sup>1</sup>School of Biosciences, University of Exeter, Exeter EX4 4PS, UK. <sup>2</sup>Rosenstiel School of Marine and Atmospheric Science, University of Miami, Miami, FL 33149–1098, USA. <sup>3</sup>University of Ottawa, Ottawa, ON K1N 6N5, Canada. <sup>4</sup>Fisheries Centre, University of British Columbia, Vancouver, BC V6T 1Z4, Canada. <sup>5</sup>Centre for Environment, Fisheries and Aquaculture Science, Lowestoft, and School of Environmental Sciences, University of East Anglia, Norwich NR4 7TJ, UK.

\*To whom correspondence should be addressed. E-mail: r.w.wilson@ex.ac.uk (R.W.W.), fmillero@rsmas.miami.edu (F.J.M.), and mgrosell@rsmas.miami.edu (M.G.)



[www.sciencemag.org/cgi/content/full/323/5912/356/DC1](http://www.sciencemag.org/cgi/content/full/323/5912/356/DC1)

Supporting Online Material for

## **Early Lunar Magnetism**

Ian Garrick-Bethell,\* Benjamin P. Weiss, David L. Shuster, Jennifer Buz

\*To whom correspondence should be addressed. E-mail: [iang@mit.edu](mailto:iang@mit.edu)

Published 16 January 2009, *Science* **323**, 356 (2008)

DOI: 10.1126/science.1166804

### **This PDF file includes:**

SOM Text

Figs. S1 to S12

Tables S1 to S3

References

## **Supplemental Online Material**

**Garrick-Bethell, I., B. P. Weiss, D. L. Shuster, J. Buz (2008) Early Lunar Magnetism, *Science*.**

### **1.0. Introduction**

Our subsamples of 76535 were collected as chips from the interior of the parent rock (76535,0) clear of any space-weathered or saw cut surfaces. Measurements of natural remanent magnetization (NRM) were performed in the MIT Paleomagnetism Laboratory (<http://web.mit.edu/paleomag>) with a 2G Enterprises Superconducting Rock Magnetometer 755 (sensitivity  $\sim 1 \times 10^{12}$  Am<sup>2</sup>) housed inside a magnetically shielded room (DC field < 150 nT). Nearly all sample handling was conducted inside a class 10,000 clean laboratory within this shielded room.

To assess the nature of the multicomponent NRM in our samples, we conducted room-temperature, three-axis alternating field (AF) demagnetization using a robotic sample handling system integrated with the magnetometer (*S1*). This automation permitted us to collect many more AF and rock magnetic measurements per sample than previous lunar experiments. Prior to this analysis our samples had been stored for 6-15 months in our magnetically shielded clean room. After AF demagnetization our samples were subjected to paleointensity analyses, selected rock magnetization experiments, hysteresis analyses, and magnetic viscosity experiments. In the following sections we describe each of these analyses and then end by providing further details about our <sup>40</sup>Ar/<sup>39</sup>Ar thermochronology calculations and our models of the thermal history of 76535.

### **2.0. Alternating field demagnetization**

To reduce spurious anhysteretic remanent magnetization (ARM) noise from our AF system (see Section 3), we performed each AF step multiple times (2-30) and computed the vector mean. A four-point vector running average was then performed on the AF measurements at progressively higher AF fields to produce the data shown in Figs. 1, S1

and S2. The reported AF field at each step is the median field of the four steps. Because we found that 76535 is susceptible to gyroremanent magnetization (GRM) (see Section 3.2), the data in Figs. 1, S1 and S2 have been corrected using the Zijderveld-Dunlop averaging method (S2). Taking the average of multiple AF steps at a single AF level also improves the accuracy of the GRM correction. The data for two of our subsamples were processed using over 1300 individual AF steps at coercivities above 25 mT (1450 steps for 138,2 and 1320 steps for 137,8).

While thermal demagnetization is traditionally the favored mechanism for assessing the remanence in terrestrial samples, there are several reasons why AF demagnetization is advantageous for lunar studies. Firstly, lunar and other extraterrestrial materials are rare, and heating permanently alters the samples such that they are often unsuitable for any subsequent petrologic and geochronological studies. While terrestrial datasets often have dozens of samples from one rock type, the mass of lunar materials typically allocated to investigators is far more limited. Previous thermal demagnetization of 76535 has shown that it alters substantially during heating (S3).

A second and related reason for using AF demagnetization is that extensive studies of rock magnetic properties can be conducted on the very same unaltered subsample that was AF demagnetized. Such studies, which can include magnetic anisotropy, acquisition of ARM and isothermal remanent magnetization (IRM), hysteresis properties, and viscous magnetization acquisition, have proven critical for determining the nature of the remanence in our samples. A third but unexpected advantage of AF demagnetization over thermal demagnetization methods is that it allowed us to identify and completely remove secondary IRM observed in 76535. The major disadvantages of performing room temperature demagnetization are AF-related noise sources like GRM and spurious-ARM, the inability to assess the blocking temperature distribution of NRM, and the inability to conduct Thellier-Thellier paleointensity analyses. Fortunately, our automated high-resolution AF demagnetizer (S1) can rapidly acquire thousands of AF measurements per sample, enabling very detailed studies of the behavior of the remanence vector and allowing us to average many measurements to reduce spurious-ARM noise, as described above.

### 3.0. Spurious remanence acquired during alternating field demagnetization

During AF demagnetization, 76535 increasingly acquires spurious remanence with growing peak AF field. This spurious remanence consists of (i) randomly oriented ARM due to imperfections in the AF equipment and (ii) GRM acquired as a result of the rock's anisotropy and our static three-axis AF protocol. The collective effect of these two artificial magnetization sources is substantial directional scatter of the NRM vector during AF demagnetization.

We can reproduce this scatter by AF demagnetizing a laboratory remanence equivalent to that inferred from our AF demagnetization of NRM experiments. For example, we applied to sample 137,1 an ARM with a DC bias field of 0.05 mT in a peak AF field of 290 mT oriented in the approximate direction of the MC component. This ARM was chosen to mimic a natural TRM acquired in a paleofield approximately equivalent in strength to that inferred from our paleointensity experiments (Fig. S3). We then rotated the sample and applied an IRM of 15 mT in the approximate direction of the LC component. AF demagnetization of this two-component remanence (ARM 0.05 mT + IRM 15mT) up to 13 mT revealed a linear monotonic decay of the vector to the approximate direction of the ARM (Fig. S4B), just as observed for NRM. The sample moment then remained in the vicinity of the ARM until at least AF 126.3 mT, with nearly identical scatter as observed for NRM in this range. The fact that this scatter is reproducible indicates that noise encountered during AF demagnetization of NRM is not inconsistent with an underlying NRM acquired in paleofields with substantial (Earth-strength or greater) paleointensities. We next explain how we substantially reduced this ARM noise and spurious GRM to recover an accurate estimate of the NRM.

*3.1. Spurious anhysteretic remanent magnetization.* It is well known that secondary harmonics in the AF waveform due to current fluctuations and imperfections in the AF equipment can cause a sample to acquire a spurious ARM (S4-8). This often appears as a random component added to the residual NRM and can be identified as directional scatter during repeat AF measurements at the same peak field. As discussed in Section 2, we



have reduced ARM noise by making repeat AF measurements (up to 30) at the same peak field, and then averaging the repeated steps.

*3.2. Gyroremanent magnetization.* During static AF demagnetization, anisotropic samples will acquire a GRM that is oriented orthogonal to the direction of the AF axis (S9). To test for GRM acquisition we conducted two experiments. In the first experiment, we compared the NRM of 76535,137,7 measured after each of three uniaxial ( $x$  (N-S),  $y$  (E-W),  $z$  (U-D)) AF steps for a given AF field. We found that above AF  $\sim 40$  mT, the moment inclination after AF in the  $z$  direction, for example, is consistently shallower (closer to the  $x$ - $y$  plane) than after AF in the  $x$  and  $y$  direction (Fig. S5A), with the degree of shallowing growing with increasing AF level. This growth in remanence in the plane orthogonal to the  $z$ -axis suggests acquisition of GRM. In the second experiment, after AF demagnetization of NRM to 290 mT we again conducted three-axis AF demagnetization of 76535,137,7 from 0 to 290 mT, following the methods of (S10). During this AF sequence, when measuring the remanence after the (final)  $z$ -axis AF demagnetization step only, we observed first a drop in sample moment followed by a rise in moment at AF levels above  $\sim 40$  mT (Fig. S5B). Like (S10), we can ascribe the initial drop in moment to AF demagnetization of GRM acquired during the last steps of our previous AF sequence (AF of NRM), and the subsequent rise in moment to progressive reacquisition of GRM in the equatorial  $x$ - $y$  plane. Note that the scatter away from these trends in Fig. S5 is very likely a manifestation of ARM noise superimposed on the GRM signal.

The results of both experiments are consistent with 76535 being susceptible to GRM acquisition during AF demagnetization. Except where noted, all measurements presented in Figs. 1, S1, S2 and used for our principal component analyses were corrected with the Zijderveld-Dunlop method (S2). Our AF demagnetization scheme proceeded in the following order:  $y$ ,  $z$ ,  $x$ ,  $y$ , and finally  $z$ . The GRM-corrected magnetization is computed as the vector average of the latter three orthogonal measurements.

## 4.0. Obtaining magnetization components

*4.1. Principal component analyses.* After AF demagnetization, low coercivity (LC), medium coercivity (MC), and high coercivity (HC) components were identified with principal component analysis (*S11*). AF demagnetization data for samples 76535,137,1 and 76535,137,8 (not shown in main text) are shown in Figs. S1 and S2. The AF steps, maximum angular deviation (MAD), anisotropy-corrected directions, and angular differences between the MC and HC components for all fits are summarized in Table S1. We note that the variability in the range of AF fields required to remove the MC component in different subsamples (from 44.5-82.9 mT) is likely a result of the inefficiency of AF demagnetization in removing two thermal components that are blocked across a mixture of coercivity levels.

Sample 76535,137,1 was only demagnetized in one axis above 85 mT, and it was therefore not possible to GRM-correct its remanence above AF 85 mT. However, above this AF level the sample shows the same well-defined origin-trending HC component as the other samples (Fig. S1B, green points). Because the HC component in 76535,137,1 manifests itself near the end of the three-axis demagnetization data (at approximately AF 83-93 mT), to obtain a fit to the HC component we used the last point in the three-axis demagnetized GRM-corrected data (AF 82.9 mT) and the origin. While such a two-point fit by itself would not be a robust measure of the final HC component, the fit passes through many points of the single-axis data that trend to the origin, which justifies its use. In addition, it produces an anisotropy-corrected angular difference between the MC and HC components that is nearly identical to the MC-HC angular differences seen in the other three samples (143.9°).

We note that while the slow cooling and blocking of the HC component in the lower crust may have produced a mixed crystallization remanent magnetization (CRM) and TRM, due to the continuing equilibration of kamacite and taenite to ~400°C (main text), the much more rapidly acquired MC component should be nearly free of any CRM effects (see also Section 6.2).

4.2. *Identifying primary magnetization.* We have argued in the main text that the HC component in 76535 is the characteristic magnetization which originated during cooling in the lower crust of the Moon. A key test of this conclusion is the demonstration that the HC component trends to origin. One such proposed quantitative test is to compute the direction of the maximum dispersion axis in the component's centroid-centered reference frame ("unconstrained line fit"), determined by PCA. The direction is then computed for a line that joins the centroid and the origin. If the angular difference between these directions, dANG, is less than some pre-defined value (e.g., the MAD for the PCA fit or else some *ad hoc* maximum threshold), then it can be said that the component trends to the origin (S12). While this kind of metric is arbitrary because it does not assign a confidence interval, the lack of more robust alternatives has led us to use it to test whether our components trend to the origin. However, instead of using the direction of the line from the centroid to the origin to compute dANG, we use the direction of the first point of the HC component, which has the advantage of weighting data further from the origin more heavily than data closer to the origin, where noise is higher. We then use the criterion of  $dANG < MAD$  to determine if HC trends to the origin, where MAD in this case is the MAD from the *unconstrained* line fit (not listed in Table S1).

We find that the HC component for sample 76535,137,8 has a dANG of  $16.2^\circ$ , which is  $< MAD = 18.5^\circ$ , and it can be said that its HC component trends to the origin. For sample 76535,137,7 we find  $dANG = 19.9^\circ$ , which is  $< MAD = 21.7^\circ$ , and it can be said that its HC component trends to the origin. For comparison, dANG for the MC component of 76535,137,7 is  $108.5^\circ$ , far greater than  $MAD = 8.5^\circ$ , and therefore its MC component does not trend to the origin, as expected. For sample 76535,138,2, we find  $dANG = 7.4^\circ$  for its HC component, which is  $< MAD = 13.0^\circ$ , and it can be said that its HC component trends to the origin. For sample 76535,137,1, only two points were used to determine the direction of HC (described above). However, if we use the non-GRM corrected single-axis demagnetized data between 94.7 and 142.0 mT (Figure S1), we find that  $dANG = 21.7^\circ$ , which is  $< MAD = 32.5^\circ$ , and therefore it can be said that its HC component trends to the origin. In summary, it can be said that all four HC components trend to the origin within the limitations of the dANG metric.

*4.3. Correction for anisotropy of remanence.* As discussed in Section 9.1, some of our subsamples of 76535 have anisotropy of remanence, which deflects their remanence directions from that of the magnetizing field. The LC, MC, and HC directions were therefore corrected for this anisotropy. For most samples, this involved computing anisotropy ellipsoids with IRM fields representative of the coercivity range of each component (10, 40, and 105 mT, for LC, MC, and HC, respectively). The anisotropy data for each sample are presented in Table S3, and the corrected directions are shown in Table S1, along with the total angular change after anisotropy correction. Sample 76535,137,7 showed negligible changes in remanence direction after correction, and the original uncorrected directions were used. In the case of 76535,138,2, the directions changed by  $\sim 10^\circ$  for all components, which led us to perform corrections using anisotropy of ARM, which is likely a better analog for TRM anisotropy. The results using ARM with a DC field of 100  $\mu$ T in AF fields of 57.0 and 120.0 mT, for the MC and HC components, respectively, yielded an MC-HC angular difference of  $141.6^\circ$ , comparable to the IRM-corrected value of  $134.4^\circ$  (a difference of  $7.2^\circ$ ). Using the MC-HC angular distance calculated from the IRM-corrected data would not affect our main conclusions.

## **5.0. Magnetic homogeneity test**

A key test of whether 76535's MC and HC components are the product of a spatially uniform external magnetic field like that of a core dynamo is that each component should be unidirectionally oriented throughout the rock (*S13*). Because our allocated subsamples of 76535 are very small, and the rock is extremely friable and not easily broken apart into mutually oriented subsamples, we used a comparison of the relative orientation of the MC and HC components as a proxy test for magnetic homogeneity. A necessary but not sufficient condition for homogeneity is that the angular distance between the two components should be constant, and indeed we observe this for all of our well-controlled subsamples of 76535 (Fig. 1G, Table S1).

We were also able to break apart one sample, 76535,138,1 into two mutually oriented subsamples (138,2, and 138,3). The two subsamples were AF demagnetized and

the directions corrected for anisotropy and GRM. After successful removal of a well-defined LC component, the demagnetization behavior of 138,3 was anomalous and unlike our other samples did not reveal clear MC or HC components, likely because of the sample's tiny size (22 mg, our smallest subsample) and relatively small number of crystals. The sample also showed particular susceptibility to GRM. We conducted a least squares fit to a possible HC component from 53.0-61.0 mT ( $MAD = 12.2^\circ$ ) that decreased monotonically in intensity from  $2.3 \times 10^{-11}$  to  $1.1 \times 10^{-11}$  Am<sup>2</sup>. After ARM anisotropy correction (DC field of 100  $\mu$ T, peak AF field of 57.0 mT), the direction of this component is  $65^\circ$  from the ARM-anisotropy corrected HC component of its pair 138,2. This angular distance is comparable to the total angular error between the two components ( $55^\circ$ ), estimated by the sum of the HC MAD values for each sample ( $11.8^\circ + 12.2^\circ$ ), the estimated relative orientation error of the two pieces ( $15^\circ$ ), and the estimated orientation errors during calculation of the anisotropy ellipsoids ( $\sim 8^\circ$  per sample), not including the formal error estimate for the anisotropy ellipsoids. Notably, the HC components of each sample moved towards each other after anisotropy correction. For comparison, the LC components (MAD values of  $0.9^\circ$  and  $4.0^\circ$ , for 138,2 and 138,3, respectively) were  $18.0^\circ$  apart after anisotropy correction using IRM fields of 10 mT. The similar LC directions for these two pieces contrasts with the non-unidirectionality of the LC components in our unoriented samples. This difference is not surprising since although IRM fields from localized sources can be highly non-uniform on the centimeter scale, they must be unidirectional below some spatial scale [typically, millimeters and below; see Fig. S1 of (S14)].

## 6.0. Paleointensity measurements

For terrestrial igneous samples, the Thellier-Thellier heating experiment is the preferred method for estimating paleofield because thermal demagnetization reproduces the way that the sample naturally acquired its NRM (S15, 16). However, numerous previous Thellier-Thellier studies of lunar rocks, including a recent such analysis of 76535, have failed to obtain accurate paleointensities due to severe sample alteration (S3, 17-20). Therefore, we made a fundamental decision to use nondestructive, order-of-magnitude

room-temperature techniques to demagnetize the NRM and obtain paleointensity estimates. Following (S14), we have normalized the NRM to a laboratory ARM and IRM rather than to a laboratory TRM like the Thellier-Thellier technique. The artificial ARM and IRM were stepwise AF demagnetized using the same AF steps as used to demagnetize the NRM, permitting us to compute NRM/ARM and NRM/IRM for each coercivity bin and therefore for each NRM component. Our paleointensity methods are therefore multicomponent techniques: our IRM method is essentially the REM' technique (S19), while our other paleointensity technique is philosophically equivalent to REM' except that ARM is used as the normalizer in place of IRM.

*6.1. Paleointensity techniques.* The IRM technique typically provides an order-of-magnitude estimate of the absolute paleofield, with the major source of error being the dependence of TRM/IRM on the unknown grain volume and microscopic coercivity distribution (S21). For example, Yu (S21) found that in terrestrial basalts, the IRM and Thellier-Thellier methods agreed within a factor of two using calibration data for meteorites, and a factor of three using the calibration for lunar samples. Weiss et al. (S22) used terrestrial basalts to find that a simple NRM/IRM metric reproduced the Earth's field within a factor of  $\sim 2$ . In addition, laboratory experiments with synthetic metal-bearing samples reproduced the ambient field within an order of magnitude for a wide range of field values (S23). However, narrow acicular shape distributions like that expected for 76535 can have TRM/IRM 50 times higher than that of equant grains (S23-25), and we incorporate this factor into our uncertainty estimates (Section 6.2).

Similar to the IRM method, NRM can also be normalized by laboratory ARM to obtain an estimate of the paleofield (S20, 26-29). Traditionally, this technique has only been applied to the total remanence. Analogous to our IRM paleointensity method, here we calculate the derivative of AF of NRM for separate magnetization components in each sample. The paleofield is obtained by multiplying NRM/ARM by the ARM bias field [ideally equal to the paleofield (S30)], and dividing by a calibration coefficient  $f'$ , which is the ratio of TRM to ARM for a given magnetizing field. There is some uncertainty in the value of  $f'$  because it changes as a function of grain size, bias field, and degree of interactions (S31), but a number of experiments have shown that a value of  $f' = 0.9$ -1.6



(typically  $f' = 1.34$ ) is fairly constant across different lunar samples (S20, 26, 32, 33). A recent analysis of ARM (S34) suggests that samples with elongate grains could have a  $f'$  perhaps 10 times larger than this. Generally, we expect the ARM method to also be accurate to within an order of magnitude (S35-37).

For each sample, we first conducted three paleointensity experiments in which ARM was acquired in increasing AF fields for constant bias fields of 50, 100, and 200  $\mu\text{T}$ . These samples were then demagnetized completely and given a near-saturation IRM (260-290 mT) that was then AF demagnetized and GRM-corrected (the multicomponent IRM method used here does not require saturating the rock because it measures remanence lost at each AF demagnetization step). We also AF demagnetized and GRM-corrected an ARM (DC bias field of 200  $\mu\text{T}$ , peak field 85 mT) to obtain a paleofield estimate analogous to the ARM acquired estimate. This was done to assess if GRM made a significant contribution to our ARM acquired paleointensity estimate (it did not). Paleointensity estimates (Table S2) were obtained from plots of NRM lost versus ARM gained [similar to the Stephenson method (S38)] and NRM lost versus IRM lost [essentially the REM' method of (S19) and REM(AF) method of (S39) but using the visualization method of (S38)]. NRM lost was computed using vector subtraction for each component. For example, for the MC component observed in 76535,137,7 (Fig. 1), NRM lost values between AF 27.6 and 72.5 mT were computed by vector subtraction from the AF 27.6 mT step, while for the HC component, NRM lost values were computed by vector subtraction from the AF 72.5 mT step. We calculated the IRM and ARM paleointensities using the following formulas:

$$\text{ARM paleointensity in } \mu\text{T} = (\Delta\text{NRM}/\Delta\text{ARM})/f' \times (\text{bias field in } \mu\text{T})$$

$$\text{IRM paleointensity in } \mu\text{T} = (\Delta\text{NRM}/\Delta\text{IRM}) \times a,$$

where  $f'$  and  $a^{-1}$  are the ratio of TRM to ARM and IRM, respectively, and  $\Delta\text{NRM}$ ,  $\Delta\text{ARM}$ ,  $\Delta\text{IRM}$  are, respectively, the vector-subtracted gain or loss of NRM, ARM, and IRM as derived from least squares fits to the paleointensity plots in the AF range for a given component. Although the uncertainty in the calibration coefficients is almost certainly higher than the uncertainty from the linear regressions to estimate the

paleofield, we also compute the 95% confidence interval for all paleofield estimates in order to demonstrate that the slopes are statistically distinguishable from zero.

Because  $f''$  and  $a$  are known to vary depending on grain size and shape, we calculated a range of paleointensities for each paleointensity method. The upper limit is obtained assuming  $f'' = 1.34$  and  $a = 3000$  (typical for equant grains of multidomain iron). The lower limit for IRM paleointensities is calculated assuming the smallest yet measured  $a = 3000/50$ . The latter value has been observed for an anorthosite from the Archean Stillwater Complex containing exsolved single-domain magnetite needles in plagioclase with aspect ratios up to 50:1 (S23); other single domain acicular magnetites as well as Fe-Ni-Co wires with axial ratios up to 14:1 also have been observed to have intermediate values of  $a$  (S24, 25). We believe  $a = 3000/50$  is a conservative lower limit on our paleointensities because although 76535 contains acicular needles of Fe-Ni-Co with axial ratios up to 45:1 (S40-42), our hysteresis data (Fig. S11) indicate that unlike the Stillwater anorthosite, the most abundant Fe-Ni metal in 76535 is in the form of approximately multidomain crystals. The latter metal is probably the large ( $\sim 10$ - $100\ \mu\text{m}$  diameter) approximately equant grains observed in the mesostasis and “mosaic assemblages” [see Fig. 6 of (S40) and Figs. 5D and 6 of (S42)]. Although the dependence of  $f''$  on shape is not well known, a recent study (S34) suggests that for magnetite with similar aspect ratios, TRM/ARM should exceed by at least the same factor of 50 as the TRM/IRM ratio that of equant grains. Therefore, we adopt a lower limit for ARM paleointensities computed using  $f'' = 1.34 \times 50$ .

**6.2. Paleointensity estimates.** Figure S3 shows the results of ARM and IRM paleointensity experiments for the MC and HC components in 76535,137,7 and 76535,138,2. The labels in each plot give the slope calculated by linear regression. Table S2 summarizes the computed slopes, formal 95% confidence intervals for the regression, and paleointensity estimates assuming the ARM and IRM calibration factors defined above. The slopes derived from GRM-corrected AF of ARM (open uncolored data points) are nearly equivalent to the slopes from the analogous ARM-acquired experiment, suggesting that GRM does not significantly affect our paleointensity estimates. In the case of 76535,137,7, the ARM acquired with a bias field of  $50\ \mu\text{T}$  was

too noisy at the coercivities blocked by the HC component (likely due to ARM noise) and did not yield a statistically significant slope.

Generally, the slopes and fields for the HC component are higher than those for the MC component. The slope changes between the two components are sharp and well defined, which suggests that the higher HC values are not due exclusively to changes in grain size or AF field but possibly to real differences in paleointensity. Note that the MC component was blocked just after the end of the period during which the HC component was acquired. While this would at first seem to suggest that the paleointensity plots should have exactly the same slope across the final AF steps of the MC component and the first AF steps of HC component, recall that upon initial excavation the rock was heated up to 600°C, which is at least ~200°C (and possibly as much as 400°C) above its final temperature acquired while in the lower crust. Therefore, given the slow cooling rate in the lower crust (several tens of °C per Ma or less), the remaining HC remanence unaffected by this reheating could be millions of years older than the MC remanence. This means there is in fact no reason to expect that the MC and HC components should have the same paleointensity. In any case, our paleointensity technique is sufficiently uncertain that it probably prevents us from accurately determining the relative strength of the MC and HC fields.

While the MC component was acquired relatively quickly, and its TRM paleointensity is likely unaffected by the effects of CRM, it is possible that the HC paleointensity is being underestimated due to the equilibration of kamacite and taenite during slow cooling to ~400°C. This is because kamacite grains will acquire some CRM as they grow during cooling, which is theoretically a less efficient magnetization process than TRM [e.g. equation 13.5 of (*S16*)]. This would effectively mean that the values used for  $a$  are lower limits and the values used for  $f'$  are upper limits. However, in the absence of experimental work on the effects of CRM on paleointensities for the Fe-Ni system, we cannot definitely determine how the HC paleointensity estimate would be affected.

As shown in Table S2, the minimum estimate from all of the paleofield experiments is 0.3-1.3  $\mu\text{T}$ . We suspect the upper range of paleointensities (in some cases exceeding 100  $\mu\text{T}$ ), which would be difficult to reconcile with the expected small size of

the lunar core (*S43*), are likely overestimates given the unusual shape distribution of metal in 76535 (see Section 6.1). The minimum paleointensities are so large that they rule out most potential field generation processes as the source of the HC and MC magnetization. Such fields are too strong to have been the product of the early T Tauri Sun (*S44*) and protoplanetary disk dynamo (*S45*) [neither of which should have been present at  $\sim 4.2$  Ga anyway (*S46*)], the solar wind or galactic field. The magnitude of fields from a dynamo on the early Earth would have also been too weak. For example, using equation 4.213 of (*S47*) to estimate the timescale for tidal growth of the lunar semimajor axis, we find that the Moon reached a semimajor axis of 20 Earth radii 0.3-30 Ma after accretion, assuming a wide range of  $k/Q = 0.1-0.001$ , where  $k$  is the Earth's second-degree tidal effective Love number and  $Q$  is its tidal specific dissipation factor (presently  $k/Q = 0.025$ ). These timescales are in agreement with timescales obtained using the treatment of (*S48*) and results reported by (*S49*). Assuming the early Earth had a dipole moment like today, its field at the Moon at 20 Earth radii would have been only  $0.006 \mu\text{T}$ , and by 4.2 Ga the Moon was almost certainly beyond 20 Earth radii. All of these field sources have the additional problem that it is difficult for them to uniformly magnetize the spinning, orbiting Moon. Lunar crustal fields like those observed today are also mostly too weak to have produced the magnetization in 76535. This leaves core dynamo fields and impact-generated fields as the two remaining explanations. As described in the main text, the well-constrained slow cooling history and lack of shock features in 76535 strongly favors a core dynamo.

## **7.0. Isothermal remanent magnetization in 76535**

During AF demagnetization of 76535, we found that all of our subsamples contained a strong, near-saturation LC component that is removed by AF  $\sim 11-13$  mT. This component is distinctly non-uniform both spatially (its orientation relative to the MC and HC components varies for different subsamples) as well as in coercivity (it is curved in orthographic plots). Similar features are observed for the IRM magnet overprints commonly found in meteorites (*S14*, *19*). The LC component also demagnetizes very similarly to a 15 mT laboratory IRM (Fig. S6). Any mismatch of the NRM with the

laboratory IRM below  $\sim 13$  mT in the samples is almost certainly due to viscous decay of the original IRM and acquisition of a terrestrial VRM. The nonlinearity of the remanence direction observed during AF demagnetization at such low fields is also probably partly due to overprinting by this VRM, as well as to the fact that natural IRM field sources are usually highly nonuniform on the sample's spatial scale (such that when the IRM source was removed from 76535, it may have progressively blocked different coercivity ranges in different directions and also produced magnetization directions varying throughout the sample). In addition, the directionality of the IRM remanence is largely controlled by anisotropy, which is greatest for low coercivity grains in 76535 (Section 9.1 and Fig. S7). All of these features strongly indicate that, like many other Apollo samples (*S3*, *50*, *51*) and meteorites (*S14*, *19*), 76535 acquired an IRM overprint prior to our analyses. The coercivity range of the IRM overprint is in the range of fields inferred to have been present in the Apollo spacecraft and also typical of hand magnets, but its true origin is unknown.

Fortunately, AF demagnetization is the ideal method for removing IRM overprints (*S50*, *52*). Six experiments on three subsamples repeatedly demonstrated that a laboratory 15 mT IRM is completely removed by AF  $\sim 12$ -13 mT [slightly less than the IRM field, presumably due to assistance by internal demagnetizing fields (*S53*)]. For example, following AF demagnetization of the NRM of 76535,137,1 to 290 mT, we applied a 15 mT IRM in the approximate LC direction and then AF demagnetized the sample again. Up to AF  $\sim 11$  mT, the laboratory IRM moment decayed monotonically with increasing AF field, and a least squares fit from AF 7.6 to 11.0 mT yielded a MAD of  $9.0^\circ$ . This behavior was similar to that of the LC component (MAD =  $9.6^\circ$  over the same AF range). By AF 14.0 mT, the remanence vector was within  $10^\circ$  of the pre-laboratory IRM direction (Fig. S4A), which was  $90.5^\circ$  away from the IRM direction. This demonstrates that the MC and HC components are unlikely to be contaminated by a low-field IRM like that which produced the LC component. These results are in agreement with a previous study (*S50*) that demonstrated how a low-field IRM from the Apollo 16 spacecraft that overprinted an Apollo 12 basalt brought back to the Moon could be essentially completely removed by AF 2 mT (as indicated by the return of the sample's moment to its pre-Apollo 16 direction).

## 8.0. Magnetic viscosity

Lunar rocks have been immersed in the Earth's magnetic field since their return during 1969-1972. It is important to establish that the MC and HC components in 76535 are not entirely VRM acquired during this period. For instance, in previous studies, fine grained iron in lunar breccias has been suspected of giving artificially high paleointensities due to recent acquisition of VRM in the Earth's field (S28, 54). In these studies, below AF fields of 10-20 mT it was found that both laboratory- and naturally acquired-VRM yielded relatively high slopes in the low coercivity portions of ARM-paleointensity plots, implying large paleofields (S28). However, at higher coercivities it was found that the slope breaks cleanly towards a shallower value that remained constant up to the limit of the demagnetizer, suggesting that VRM was removed and that the high coercivity magnetization components represented primary remanence (S28). These results are also in agreement with similar VRM experiments on breccias by (S55), where terrestrial VRM was removed by AF ~20 mT.

We also find marked direction changes and suspected VRM components that are removed by at most AF 10 mT. Consider 76535,137,1, which from a comparison of AF demagnetization of NRM and IRM 15 mT has by far the largest VRM component of all of our subsamples (Figs. S1A, S6B). The responsibility of low coercivity grains for the VRM is clearly demonstrated by (a) the directional change and decay of the LC component at AF 3.6 mT and near 8.2 mT and by (b) the relatively small amount of NRM lost by AF 15 mT relative to that lost by a 15 mT IRM. Because the LC component was apparently viscously affected only in grains with coercivities <8.2 mT and was directionally stable between AF 8.2-11 mT (and compared favorably with low-field laboratory IRM) despite years of storage in the Earth's field, we can be confident that higher coercivity grains have not been affected by VRM.

We tested this conclusion by conducting our own VRM-acquisition experiments on 76535. Three subsamples were exposed to the Earth's field after AF demagnetization of NRM up to 290 mT. Two of these subsamples (76535,137,3 and 137,5) exhibited little apparent viscous demagnetization of their natural LC IRM during AF



demagnetization of their NRM. During the subsequent artificial VRM experiments, these samples indeed showed no detectable evidence of VRM ( $<1\%$  of the sample's pre-VRM moment) after exposure to the Earth's field for 42 days (measured within 100 s of reentry into the shielded room). On the other hand, sample 137,1, which as described above exhibits the effects of substantial natural viscous demagnetization of its LC IRM, acquired after 42 days of Earth-field exposure a moment of  $3.2 \times 10^{-10} \text{ Am}^2$ , which is 44% of its NRM, 60% of the NRM lost up to AF 8.2 mT ( $5.4 \times 10^{-10} \text{ Am}^2$ ), and 73% of its pre-VRM moment. If VRM acquisition is approximated as linear with the logarithm of time, the predicted VRM after 10 years of undisturbed storage at Johnson Space Center and 6 months of storage in a shielded room would be  $0.6 \times 10^{-10} \text{ Am}^2$ . This is only 11% of the NRM lost up to AF 8.2 mT. However, this is not unexpected given that VRM acquisition is nonlinear with time (S56) and the LC component is a mixture of IRM and VRM. No detectable change ( $<1\%$ ) from the post-VRM moment was observed during 100 continuous measurements performed over one hour after removal from the Earth's field. However, after 7 days of storage in a shielded room the moment of 137,1 had returned to 96.5% of its original value, and after 23 days the sample moment had returned completely to its previous magnitude (99%) and direction ( $3^\circ$ ), suggesting a very soft component of low coercivity grains was the carrier of the VRM, as observed for other lunar samples.

## 9.0. Other rock magnetic data

*9.1. Anisotropy of remanence.* 76535 is a coarse grained rock with plagioclase and olivine crystal sizes ranging from  $\sim 0.2$  to  $\sim 3$  mm in diameter. The relatively small size of our analyzed subsamples means that they each contain several dozen or fewer olivine and plagioclase crystals. The plagioclase contains oriented arrays and needles (with axial ratios sometimes exceeding  $>50$ ) of metallic inclusions (S40-42). This would suggest that our subsamples could exhibit significant anisotropy of remanence. Such anisotropy would influence the remanence directions inferred from our PCA fits [i.e., (S57)] as well as the magnitude of our paleointensity analyses [i.e., (S58)].

To characterize the anisotropy of remanence, we applied an IRM in three orthogonal directions and then solved for the principal axes of the IRM anisotropy ellipsoid following (S59, 60). We conducted this experiment for at least four different IRM fields (10, 40, 105 and 205 mT) in order to determine how the anisotropy varies as a function of coercivity. Table S2 summarizes some of the data at fields relevant for the LC, MC, and HC components. We found that the degree of anisotropy,  $P$  (S61) decreases monotonically as coercivity increases for all samples, suggesting that anisotropy of higher coercivity grains is lower than those of lower coercivity. The continually changing anisotropy as a function of coercivity could be responsible for some of the deviations from ideal linear demagnetization observed in Figs. 1, S1 and S2. The shape factor  $T$  (S62), was generally positive, indicating that the anisotropy ellipsoid is oblate.

The directions of the LC components with respect to the principal anisotropy axes are a direct manifestation of the high anisotropy carried by low coercivity grains described above. The LC component directions for all seven samples are either close to the easy axis direction or in the easy-intermediate plane as computed from a low field IRM. There is no such trend for the MC and HC components. Figure S7 shows the uncorrected LC directions and the first, second, and third principal axes of the anisotropy ellipsoids calculated with an IRM of 10 mT. Three LC components cluster very close to the sample's first axis, and the remaining four points lie within or near the easy-intermediate plane. This strong correlation of the IRM with anisotropy axes is consistent with other findings in meteorites and lunar rocks (S63). However, in this case the anisotropy is not due to shock related processes, but rather the rock's naturally coarse grain size.

*9.2. Anhysteretic remanent magnetization and isothermal remanent magnetization acquisition and demagnetization.* Samples 76535,137,3 and 137,5 were given stepwise ARM in increasing DC bias fields from 0.5 to 2 mT in a peak AC field of 200 mT (Fig. S8). These data can be used to infer the degree of magnetostatic interactions in the sample (S53). Following ARM acquisition, the ARM was then stepwise AF demagnetized, and the median destructive field was found to be 13.5 and 11.0 mT for

137,3 and 137,5, respectively. The samples were then given an IRM with a DC field of 200 mT that was also subsequently stepwise AF demagnetized (Fig. S9), and the median destructive field was found to be 13.5 and 11.2 mT, for 137,3, and 137,5, respectively. The IRM acquisition and AF demagnetization of IRM data are indicators of the coercivity spectrum of the sample. Comparison of the AF demagnetization of ARM and IRM constitutes the Lowrie-Fuller test (Fig. S10), an indicator of grain size and stress state (S64, 65). The data indicate that the rock exhibits H-type (IRM more stable than ARM) behavior, consistent with kamacite and ferromagnetic taenite in the pseudo single domain to multidomain size range (see also Section 9.3).

High ARM susceptibility (Fig. S7) and Cisowski  $R$  values (S53) ranging from 0.42-0.44 (Fig. S9) indicate that 76535 contains relatively weakly interacting grains or some multidomain grains. IRM acquisition and demagnetization data (Fig. S8) and coercivity of remanence values (18.5, 16.0, and 36.0 mT for 137,3, 137,5, and 137,1, respectively) are consistent with the presence of kamacite and taenite [and not the high coercivity mineral tetrataenite (S66, 67)] as the main ferromagnetic phases in 76535.

*9.3. Hysteresis loops.* Room temperature hysteresis data for 76535,137,1 and 76535,137,3 were obtained with a Digital Measurement Systems vibrating sample magnetometer in C. Ross's laboratory in the MIT Department of Materials Science and Engineering. The high-field slope of each hysteresis loop was used to estimate the contribution of paramagnetic and diamagnetic minerals. Their contribution has been subtracted from the loops shown in Fig. S11. We found that the subsample containing significant amounts of both olivine and plagioclase (137,1) is predominantly multidomain (Fig. S11A), with a ratio of saturation remanence to saturation magnetization  $M_{rs}/M_s = 0.016$  and a ratio of coercivity of remanence to coercivity of  $H_{cr}/H_c = 9$  [see (S68), with the caveat that the results of this study are formally only applicable to magnetite]. On the other hand, the very plagioclase-rich sample (137,3) is apparently pseudo-single domain, with  $M_{rs}/M_s = 0.027$  and  $H_{cr}/H_c = 3$  (Fig. S11B). The latter is the first lunar plutonic rock sample observed to have such fine-grained remanence carriers and is in fact one of the most single-domain like lunar samples known [see (S51)]. This may be because the metal in this sample is likely mostly in the form of exsolved needle-shaped inclusions in

the plagioclase, whereas the metal in 137,1 may be in larger interstitial grains. The observed saturation field near 1 T and the  $M_{rs}/M_s$  and  $H_{cr}/H_c$  values indicate that kamacite and taenite rather than tetrataenite (S66, 67) are the major ferromagnetic phases in 76535. This is also consistent with the thermal history of the rock (Fig. 2), during which any tetrataenite formed during slow cooling in the lunar crust should have been destroyed upon heating to  $\sim 500^\circ\text{C}$  and cooling over 10 ka in an ejecta blanket [i.e., (S67, 69-74)].

## 10.0. $^{40}\text{Ar}/^{39}\text{Ar}$ thermochronology

Three different groups have dated 76535 using K/Ar and  $^{40}\text{Ar}/^{39}\text{Ar}$  geochronology and have obtained plateau and integrated ages ranging from 4.2-4.3 Ga (S75-77). The most thoroughly documented of these studies is that of Husain and Schaeffer (S77). We used their data to conduct  $^{40}\text{Ar}/^{39}\text{Ar}$  thermochronology calculations in order to constrain the temperature history of the 76535. Using their plagioclase  $^{39}\text{Ar}$  release data assuming that their heating steps lasted  $\sim 1$  h (S78, 79), we calculated the temperature-dependence of the  $^{39}\text{Ar}$  diffusion coefficients  $D(T)$  through 76535 assuming a spherical diffusion domain geometry (Fig. 3A). We then conducted thermochronological modeling following our previous analyses of Martian meteorites (S80-82). We assumed that the colinearity observed for the first 6 heating steps (1000-1350 $^\circ\text{C}$ ) of the released  $^{39}\text{Ar}$  indicates that the diffusion of Ar in 76535 plagioclase is thermally activated over this range. Assuming the diffusivity is described by an Arrhenius relationship, a least squares regression to these data gave an activation energy  $E_a = 236.9 \pm 27.6$  kJ mol $^{-1}$  and  $\ln(D_0/a^2) = 4.43 \pm 0.95$  ln(s $^{-1}$ ) for diffusivity at infinite temperature  $D_0$  and diffusive length scale  $a$ . This diffusivity is at the retentive end of that typically observed for plagioclase (S83, 84).

Consistent with the lack of deformational textures in this rock, we assume that this Arrhenius relationship and corresponding diffusive length scale,  $a$ , have held for 76535 since the deep crustal metamorphic event. Using a numerical solution to the radiogenic production-diffusion equation described by (S82, 85) and using a radius of 2.5 cm for the parent rock (S82, 86), we simulated the expected radiogenic  $^{40}\text{Ar}$  ( $^{40}\text{Ar}^*$ ) distributions within the sample following various thermal perturbations at 3.9 Ga (the putative late heavy bombardment) and 220 Ma [the time of recent excavation of 76535 given by its

cosmic ray exposure age (S87)]. We found that there is *no evidence for any  $^{40}\text{Ar}$  loss since 4.2 Ga*. From this we derived a *conservative upper bound* on the time-temperature history for thermal events at 3.9 Ga and 220 Ma assuming no gas loss at any other time in the rock's history (Fig. 3C).

## 11.0. Conductive cooling timescales

As described in the main text, establishing the conductive heating and cooling timescale for 765335 is critical for establishing the origin and duration of the field that magnetized it. We have already established that the rock could not have been shock heated (see main text). Quick heating and cooling ( $< 1$  day) as a result of heating in an impact ejecta blanket might permit the rock to acquire a TRM from any associated impact-generated fields (which are thought to persist for as long as  $\sim 1$  day for the largest, basin-forming impacts), while slower heating and cooling would mean that impact-generated fields would not be present long enough to block a TRM. To determine the typical conductive heating and cooling timescales for 76535, we modeled the rock as a sphere of radius  $R$  at initial temperature  $T_0$  surrounded by an infinite medium with initial temperature  $T$ . The temperature at a radius  $r$  within the sphere can then be computed using equation (6) from Section 10.2 of (S88) [see also (S82)]. For these calculations, we assumed a thermal diffusivity of  $10^{-6} \text{ m}^2\text{s}^{-1}$ , a specific heat of  $815 \text{ J kg}^{-1} \text{ K}^{-1}$ , and a density of  $2800 \text{ kg m}^{-3}$ . Fig. S12 shows the heating time for a rock with  $T_0 = -20^\circ\text{C}$ , the approximate lunar near-surface temperature at depths not subject to diurnal fluctuations (S89), to reach a temperature of  $T = 770^\circ\text{C}$ , the Curie temperature of pure iron, at a radius of  $r = R/2$ , for several values of  $R$ . During this time, the rock could not acquire magnetization, yet any impact-generated fields would be decaying. An extreme minimum heating timescale for 76535 can be computed using only the size of the rock recovered by the Apollo astronauts ( $R = 2.5 \text{ cm}$ ). For this radius, we find that the rock will heat up to the ambient temperatures of an ejecta blanket in  $\sim 1000 \text{ s}$ , long compared to the expected lifetimes of impact-generated and -amplified fields. Fig. S12 also shows the time required for conductive cooling of a rock, which is representative of the cooling timescale for an ejecta blanket. The total time required for the rock to acquire TRM is the sum of both the

heating and cooling times. Even very small ejecta blankets of  $\sim 1$  m diameter would remain hot for  $\sim 1$  day.



## References

- S1. J. L. Kirschvink, R. E. Kopp, T. D. Raub, C. T. Baumgartner, J. W. Holt, *Geochem. Geophys. Geosys.* **9**, Q05Y01 (2008).
- S2. A. Stephenson, *J. Geophys. Res.* **98**, 373 (1993).
- S3. K. P. Lawrence, C. L. Johnson, L. Tauxe, J. Gee, *Phys. Earth Planet. Inter.*, doi:10.1016/j.pepi.2008.05.007 (2008).
- S4. C. Snape, *Geophys. J. R. Astr. Soc.* **23**, 361 (1971).
- S5. E. A. Hailwood, L. Molyneux, *Geophys. J. R. Astr. Soc.* **39**, 421 (1974).
- S6. D. W. Collinson, *Methods in Rock Magnetism and Paleomagnetism*. (Chapman and Hall, New York, N.Y., 1983), pp. 503.
- S7. S. J. Morden, *Phys. Earth. Planet. Inter.* **71**, 189 (1992).
- S8. G. Acton *et al.*, *J. Geophys. Res.* **112**, doi:10.1029/2006JB004655 (2007).
- S9. A. Stephenson, *J. Geophys. Res.* **98**, 373 (1993).
- S10. S. Hu, E. Appel, V. Hoffmann, W. W. Schmahl, S. Wang, *Geophys. J. Int.* **134**, 831 (1998).
- S11. J. L. Kirschvink, *Geophys. J. R. Astr. Soc.* **62**, 699 (1980).
- S12. L. Tauxe, H. Staudigel, *Geochem. Geophys. Geosyst.* **5**, doi:10.1029/2003GC000635 (2004).
- S13. D. W. Collinson, *Earth Moon Planet.* **33**, 31 (1985).
- S14. B. P. Weiss *et al.*, *Science*, in press (2008).
- S15. E. Thellier, O. Thellier, *Ann. Geophys.* **15**, 285 (1959).
- S16. D. J. Dunlop, O. Ozdemir, *Rock Magnetism: Fundamentals and Frontiers*. (Cambridge University Press, 2001).
- S17. M. Westphal, *Phys. Earth Planet. Inter.* **43**, 300 (1986).
- S18. J. R. Dunn, M. Fuller, D. Clauter, *Proc. Lunar Planet. Sci. Conf. 12th*, 1747 (1981).
- S19. J. Gattacceca, P. Rochette, *Earth Planet. Sci. Lett.* **227**, 377 (2004).
- S20. K. A. Hoffman, J. R. Baker, S. K. Banerjee, *Phys. Earth Planet. Inter.* **20**, 317 (1979).
- S21. Y. Yu, *Earth Planet. Sci. Lett.* **250**, 27 (2006).
- S22. B. P. Weiss, E. A. Lima, L. E. Fong, F. J. Baudenbacher, *Earth Planet. Sci. Lett.* **264**, 61 (2007).
- S23. G. Kletetschka *et al.*, *Phys. Earth Planet. Inter.* **154**, 290 (2006).
- S24. G. Kletetschka, M. H. Acuna, T. Kohout, P. J. Wasilewski, J. E. P. Connerney, *Earth Planet. Sci. Lett.* **226**, 521 (Oct 15, 2004).
- S25. Y. Yu, L. Tauxe, J. S. Gee, *Phys. Earth Planet. Inter.* **162**, 244 (2007).
- S26. A. Stephenson, D. W. Collinson, *Earth Planet Sci. Lett.* **23**, 220 (1974).
- S27. A. Stephenson, S. K. Runcorn, D. W. Collinson, *Proc. Lunar Sci. Conf. 8th*, 679 (1977).
- S28. N. Sugiura, D. W. Strangway, *Proc. Lunar Planet. Sci. Conf. 11th*, 1801 (1980).
- S29. S. J. Morden, *Phys. Earth Planet. Inter.* **71**, 189 (1992).
- S30. M. E. Bailey, D. J. Dunlop, *Phys. Earth Planet. Inter.* **13**, 360 (1977).
- S31. S. Levi, R. T. Merrill, *Earth Planet. Sci. Lett.* **32**, 171 (1976).
- S32. A. Stephenson, D. W. Collinson, S. K. Runcorn, *Proc. Lunar Sci. Conf. 7th*, 3373 (1976).
- S33. T. Nagata, *Proc. Lunar Planet. Sci. Conf. 10th*, 2199 (1979).

- S34. R. Egli, W. Lowrie, *J. Geophys. Res.* **107**, doi:10.1029/2001JB000671 (2002).
- S35. D. J. Dunlop, K. S. Argyle, *J. Geophys. Res.* **102**, 20199 (1997).
- S36. D. J. Dunlop, M. E. Bailey, M. F. Westcott-Lewis, *Proc. Lunar Sci. Conf. 6th*, 3063 (1975).
- S37. S. Levi, R. T. Merrill, *Earth Planet Sci. Lett.* **32**, 171 (1976).
- S38. A. Stephenson, D. W. Collinson, S. K. Runcorn, *Proc. Tenth Lunar Planet. Sci. Conf.*, 2859 (1974).
- S39. T. Kohout, G. Kletetschka, F. Donadini, M. Fuller, E. Herrero-Bervera, *Stud. Geophys. Geod.* **52**, 225 (2008).
- S40. R. Gooley, R. Brett, J. R. Smyth, J. Warner, *Geochim. Cosmochim. Acta* **38**, 1329 (1974).
- S41. G. L. Nord, *Proc. Lunar Sci. Conf. 7th*, 1875 (1976).
- S42. R. F. Dymek, A. L. Albee, A. A. Chodos, *Proc. Lunar Sci. Conf. 6th*, 301 (1975).
- S43. M. A. Wicczorek *et al.*, *Reviews in Mineralogy and Geochemistry* **60**, 221 (2006).
- S44. J.-P. Vallée, *New Astron. Rev.* **47**, 85 (2003).
- S45. S. A. Balbus, *Annu. Rev. Astron. Astrophys.* **41**, 555 (2003).
- S46. S. S. Russell *et al.*, in *Meteorites and the Early Solar System II*, D. S. Lauretta, H. Y. McSween, Eds. (University of Arizona, Tucson, 2006), pp. 233-251.
- S47. C. D. Murray, S. F. Dermott, *Solar system dynamics*. (Cambridge University Press, Cambridge, 2000), pp. 606.
- S48. F. Mignard, *Moon and Planets* **23**, 185 (1980).
- S49. S. J. Peale, P. Cassen, *Icarus* **36**, 245 (1978).
- S50. G. W. Pearce, D. W. Strangway, *Apollo 16: Preliminary Science Report. NASA SP-315, Ch. 7-55*, (1972).
- S51. M. Fuller, S. M. Cisowski, *Geomagnetism* **2**, 307 (1987).
- S52. F. Rimbart, *Ph.D. Thesis, University of Paris*, (1958).
- S53. S. M. Cisowski, *Phys. Earth Planet. Inter.* **26**, 56 (1981).
- S54. D. J. Dunlop, *Rev. Geophys. Space Phys.* **11**, 855 (1973).
- S55. W. A. Gose, G. W. Pearce, D. W. Strangway, E. E. Larson, *Moon* **5**, 106 (1972).
- S56. Y. Yu, L. Tauxe, *Phys. Earth Planet. Inter.* **159**, 32 (2006).
- S57. H. Hyodo, D. J. Dunlop, *J. Geophys. Res.* **98**, 7997 (1993).
- S58. P. A. Selkin, J. S. Gee, L. Tauxe, W. P. Meurer, A. J. Newell, *Earth Planet. Sci. Lett.* **183**, 403 (2000).
- S59. A. Stephenson, S. Sadikun, D. Potter, K., *Geophys. J. R. Astr. Soc.* **84**, 185 (1986).
- S60. J. F. Nye, *Physical Properties of Crystals: Their Representation by Tensors and Matrices*. (Oxford University Press, Oxford, 1985).
- S61. T. Nagata, *Rock Magnetism*. (Maruzen Company, Tokyo, 1961), pp. 350.
- S62. V. Jelinek, *Tectonophysics* **79**, 63 (1981).
- S63. J. Gattacceca, P. Rochette, M. Bourot-Denise, *Phys. Earth Planet. Inter.* **140**, 343 (2003).
- S64. W. Lowrie, M. Fuller, *J. Geophys. Res.* **76**, 6339 (1971).
- S65. S. Xu, D. J. Dunlop, *J. Geophys. Res.* **100**, 22533 (1995).
- S66. T. Nagata, *Proc Lunar Planet. Sci. Conf. 13*, A779 (1983).
- S67. P. Wasilewski, *Phys. Earth Planet. Inter.* **52**, 150 (1988).
- S68. D. J. Dunlop, *J. Geophys. Res.* **107**, doi:10.1029/2001JB000486 (2002).

- S69. L. Larsen, H. Roy-Paulsen, N. O. Roy-Paulsen, L. Vistisen, *Phys. Rev. Lett.* **48**, 1054 (1982).
- S70. J. F. Petersen, M. Aydin, J. M. Knudsen, *Phys. Lett.* **62A**, 192 (1977).
- S71. J. F. Albertsen, M. Aydin, J. M. Knudsen, *Phys. Scripta* **17**, 467 (1978).
- S72. R. Gooley, R. B. Merrill, J. R. Smyth, *Meteoritics* **10**, 410 (1975).
- S73. S. J. Morden, D. W. Collinson, *Earth Planet. Sci. Lett.* **109**, 185 (Mar, 1992).
- S74. T. Nagata, *Proc. Lunar Planet. Sci. Conf. 13th*, A779 (1983).
- S75. D. D. Bogard, L. E. Nyquist, B. M. Bansal, H. Wiesmann, C.-Y. Shih, *Earth Planet. Sci. Lett.* **26**, 69 (1975).
- S76. J. C. Huneke, G. J. Wasserburg, *Lunar Sci. VI*, 417 (1975).
- S77. L. Husain, O. A. Schaeffer, *Geophys. Res. Lett.* **2**, 29 (1975).
- S78. L. Husain, *Science* **175**, 428 (1972).
- S79. L. Husain, *J. Geophys. Res.* **79**, 19 (1974).
- S80. H. Fechtig, S. T. Kalbitzer, in *Potassium Argon Dating*, O. A. Schaeffer, J. Zähringer, Eds. (Springer-Verlag, New York, 1966), pp. 68-107.
- S81. D. L. Shuster, B. P. Weiss, *Science* **309**, 594 (2005).
- S82. B. P. Weiss, D. L. Shuster, S. T. Stewart, *Earth Planet. Sci. Lett.* **201**, 465 (2002).
- S83. W. A. Cassata, P. R. Renne, D. L. Shuster, *Goldschmidt Conf. Abs.*, A142 (2008).
- S84. I. McDougall, M. T. Harrison, *Geochronology and thermochronology by the  $^{40}\text{Ar}/^{39}\text{Ar}$  method*. (Oxford University Press, 1999), pp. 269.
- S85. D. L. Shuster, K. A. Farley, *Earth Planet. Sci. Lett.* **217**, 1 (2004).
- S86. O. Eugster, H. Busemann, S. Lorenzetti, D. Terrebilini, *Meteorit. Planet. Sci.* **37**, 1345 (2002).
- S87. G. W. Lugmair, K. Marti, J. P. Kurtz, N. B. Scheinin, *Proc. Lunar Sci. Conf. 7th*, 2009 (1976).
- S88. H. S. Carslaw, J. C. Jaeger, *The conduction of heat in solids*. (Oxford University Press, London, 1959).
- S89. G. H. Heiken, D. T. Vaniman, B. M. French, *Lunar Sourcebook: A User's Guide to the Moon*. (Cambridge University Press, London, 1991), pp. 756.

**Table S1** – Summary of magnetization components from principal component analysis and corrected directions from anisotropy of remanence computed using IRM fields of 10, 40, and 105 mT for LC, MC, and HC, respectively, except where indicated. MAD = maximum angular deviation.

Sample, component	AF range (mT)	Fit type *	Dec., Inc. (°)	Dec., Inc. anisotropy-corrected (°)	Angular change (°)†	MC-HC distance (°)	MAD (°)	Points
76535,137,1								
LC	7.6-10.5	L	104.9, 34.2	100.5, 28.4	6.9	-	9.6	6
MC	35.9-82.9	L	176.6, 54.5	156.8, 48.9	13.4	-	25.7	18
HC	82.9-origin‡	AL	40.7, -62.5	40.3, -67.5	5.0	143.9	-	2
76535,137,7								
LC	8.9-11.3	L	359.5, 73.2	Neg.§	0	-	3.2	7
MC	27.6-72.5	L	206.9, 71.3	Neg.§	0	-	8.5	10
HC	72.5-252.5	AL	47.2, -41.0	Neg.§	0	148.0	6.5	12
76535,137,8								
LC	6.8-11.8	L	226.0, -44.5	229.3, -47.9	4.1	-	2.8	11
MC	19.8-34.5	L	152.6, 57.4	159.4, 55.3	4.3	-	20.9	5
HC	44.5-205.0	AL	22.9, -41.4	23.7, -42.6	1.3	148.9	14.1	22
76535,138,2								
LC	6.8-11.8	L	335.5, -57.1	8.0, -34.0	31.9	-	0.9	11
MC	25.0-59.0	L	178.8, 69.4	198.6, 56.5	15.6	-	19.4	17
HC	59.0-172.5	AL	59.5, -36.8	46.8, -24.0	16.8	141.6	11.8	28

\* Fit type: L = line. AL = line anchored to the origin.

† Difference between directions before and after anisotropy correction.

‡ Only one measurement point used in fit. See text for details.

§ Negligible change (less than 2°).

|| Remanence corrected with ARM(100  $\mu$ T) at peak AC fields of 57 and 120 mT for MC and HC, respectively. Remanence corrected with IRM(57 mT) and IRM(120 mT) gives similar angular changes (8.9° and 12.7°) in the same directions, with an MC-HC angular distance of 134.4°.

**Table S2:** Paleointensity estimates for medium coercivity (MC) and high coercivity (HC) components in 76535. See Section 6 for details.

Sample, Experiment	MC slope	Paleointensity ( $\mu$ T)	HC slope	Paleointensity ( $\mu$ T)*
76535,137,7				
ARM 50 $\mu$ T	0.68 $\pm$ 0.23	0.50 $\pm$ 0.2 to 25 $\pm$ 8	-	-
ARM 100 $\mu$ T	0.38 $\pm$ 0.09	0.56 $\pm$ 0.1 to 28 $\pm$ 7	0.53 $\pm$ 0.18	0.8 $\pm$ 0.2 to 40 $\pm$ 10
ARM 200 $\mu$ T	0.22 $\pm$ 0.04	0.64 $\pm$ 0.1 to 32 $\pm$ 7	0.42 $\pm$ 0.14	1.2 $\pm$ 0.4 to 62 $\pm$ 20
AF ARM† 200 $\mu$ T	0.22 $\pm$ 0.07	0.66 $\pm$ 0.2 to 33 $\pm$ 10	-	-
AF IRM†	0.019 $\pm$ 0.004	1.2 $\pm$ 0.2 to 58 $\pm$ 10	0.058 $\pm$ 0.01	3.5 $\pm$ 0.6 to 170 $\pm$ 30
76535,138,2				
ARM 50 $\mu$ T	0.36 $\pm$ 0.035	0.26 $\pm$ 0.02 to 13 $\pm$ 1	1.50 $\pm$ 0.30	1.2 $\pm$ 0.2 to 58 $\pm$ 10
ARM 100 $\mu$ T	0.23 $\pm$ 0.04	0.34 $\pm$ 0.06 to 17 $\pm$ 3	1.50 $\pm$ 0.40	2.2 $\pm$ 0.6 to 110 $\pm$ 30
ARM 200 $\mu$ T	0.11 $\pm$ 0.02	0.32 $\pm$ 0.04 to 16 $\pm$ 2	0.86 $\pm$ 0.08	2.6 $\pm$ 0.2 to 130 $\pm$ 10
AF ARM† 200 $\mu$ T	0.12 $\pm$ 0.02	0.38 $\pm$ 0.06 to 19 $\pm$ 3	0.73 $\pm$ 0.08	2.2 $\pm$ 0.2 to 110 $\pm$ 10
AF IRM†	0.02 $\pm$ 0.003	1.3 $\pm$ 0.2 to 66 $\pm$ 8	0.13 $\pm$ 0.02	7.9 $\pm$ 1.0 to 390 $\pm$ 50

Note: ARM paleointensity in microteslas = (NRM/ARM)/ $f'$   $\times$  (bias field in microteslas), and IRM paleointensity in microteslas = NRM/IRM  $\times$   $a$ . The limits of the given paleointensity range were computed using two extreme values of  $f'$  = 1.34 and 1.34 $\times$ 50 and  $a$  = 3000 and 3000/50. Uncertainties on each limit are formal 95% confidence intervals on the slope fit using Student's  $t$ -test.

\* These values may be lower limits given the possible contribution of phase transformation crystallization remanent magnetization to the HC component.

† GRM-corrected.

**Table S3.** Anisotropy of remanence data for 76535, at IRM fields of 10, 40, and 105  $\mu\text{T}$ .  $P$  = degree of anisotropy.  $T$  = shape factor.

Sample	Mass (mg)	NRM ( $\text{Am}^2$ )	$P$ (10 $\mu\text{T}$ )	$T$ (10 $\mu\text{T}$ )	$P$ (40 $\mu\text{T}$ )	$T$ (40 $\mu\text{T}$ )	$P$ (105 $\mu\text{T}$ )	$T$ (105 $\mu\text{T}$ )
76535,137,1	68	$7.20 \times 10^{-10}$	2.79	-0.32	1.89	-0.36	1.50	-0.32
76535,137,3	55	$7.73 \times 10^{-9}$	5.00	0.15	4.14	0.04	3.00	-0.30
76535,137,7	109	$2.32 \times 10^{-9}$	1.22	0.80	1.16	-0.49	1.10	0.33
76535,137,8	48	$3.39 \times 10^{-9}$	1.56	-0.04	1.39	0.82	1.44	0.25
76535,138,2	38	$1.41 \times 10^{-9}$	3.31	-0.08	2.27	0.31	1.65	0.43
76535,138,3	22	$5.82 \times 10^{-10}$	2.61	0.41	1.93	0.24	1.18	-0.29

## Figure Captions

**Fig. S1.** Natural remanent magnetization in 76535,137,1. (A, B) two-dimensional projection of the NRM vector during AF demagnetization. Closed (open) symbols represent end points of magnetization projected onto horizontal N-E (vertical N-Z) planes. Peak fields for selected AF steps are labeled in mT. Dashed lines are component directions determined from principal component analyses. (A) AF demagnetization up to 89.2 mT and the LC component. (B) Zoom of boxed region in part A, showing MC (blue) and HC (red) components, determined from a total of 80 AF measurements. The HC fit is anchored to the origin. Green points show data that are not GRM corrected and only AF demagnetized in one axis above 85.0 mT (not used in any fits). (C) Equal area projection of the remanence shown in part A.

**Fig. S2.** Natural remanent magnetization in 76535,137,8. (A, B) two-dimensional projection of the NRM vector during AF demagnetization. Closed (open) symbols represent end points of magnetization projected onto horizontal N-E (vertical N-Z) planes. Peak fields for selected AF steps are labeled in mT. Dashed lines are component directions determined from principal component analyses. (A) AF demagnetization up to 205.0 mT and the LC component. (B) Zoom of boxed region in part A, showing MC (blue) and HC (red) components, determined from a total of 1320 AF measurements. The HC fit is anchored to the origin. (C) Equal area projection of the remanence shown in part A.

**Fig. S3.** Paleointensity estimates for 76535. Slopes derived from linear regressions are shown next to each experiment. Blue and red points correspond to the MC and HC fits and AF steps identified in Table S1. (A, B) ARM method paleointensity estimates for 76535,137,7 and 76535,138,2. Open, uncolored points are GRM-corrected AF of ARM measurements for the MC and HC components of 76535,138,2, and the MC component of 76535,137,7, performed for AF steps below 85.0 mT. (C, D) IRM method paleointensity estimates for 76535,137,7 and 76535,138,2. AF of IRM experiment data are GRM corrected.



**Fig. S4.** AF demagnetization of IRM and ARM in 76535,137,1. (A) AF demagnetization of a laboratory 15 mT IRM after demagnetization of NRM, applied 90.5° away from the pre-IRM direction. (B) AF demagnetization of a laboratory ARM (0.05 mT bias field in a peak AF field of 290 mT), plus a subsequent laboratory 15 mT IRM, both applied after demagnetization of NRM.

**Fig. S5.** Evidence for gyroremanent magnetization (GRM) acquisition by 76535,137,7. (A) Difference between the average inclination of moment following uniaxial AF demagnetization in the  $x$ - and  $y$ -directions and that in the  $z$ -direction, as observed during NRM demagnetization. Above ~40 mT, the moment after demagnetization in the  $z$ -direction is increasingly shallower than after demagnetization in the horizontal directions (difference > 0 as shown by dashed line). This is consistent with GRM, which is acquired perpendicular to the AF axis. (B) Alternating field demagnetization experiment following (S10). Prior to the first AF step, sample NRM had been demagnetized up to 290 mT during which it acquired a GRM. This GRM is steadily demagnetized up to at least 40 mT. Beyond 40 mT, a new GRM is steadily acquired.

**Fig. S6.** Remanence magnitude of 76535 during AF demagnetization. Shown is the moment as a function of peak AF field for natural remanent magnetization (NRM) (blue curves), isothermal remanent magnetization (IRM) (red and green curves), and anhysteretic remanent magnetization (purple). IRM field and ARM DC bias fields in mT are labeled. The peak ARM fields for all curves were 250 mT. (A) Subsample 76535,137,3. (B) Subsample 76535,137,3. (C) Subsample 76535,137,7.

**Fig. S7.** Stars represent the first, second, and third anisotropy ellipsoid axes for all subsamples, determined by IRM 10 mT. Circles are the LC components for each subsample (generally fit between AF steps 6-12 mT, see Table S1) in the same coordinate system as the anisotropy ellipsoid.

**Fig. S8.** Anhysteretic remanent magnetization (ARM) acquisition experiments on selected subsamples of 76535. Shown is the ARM acquired in a 200 mT AC field as a

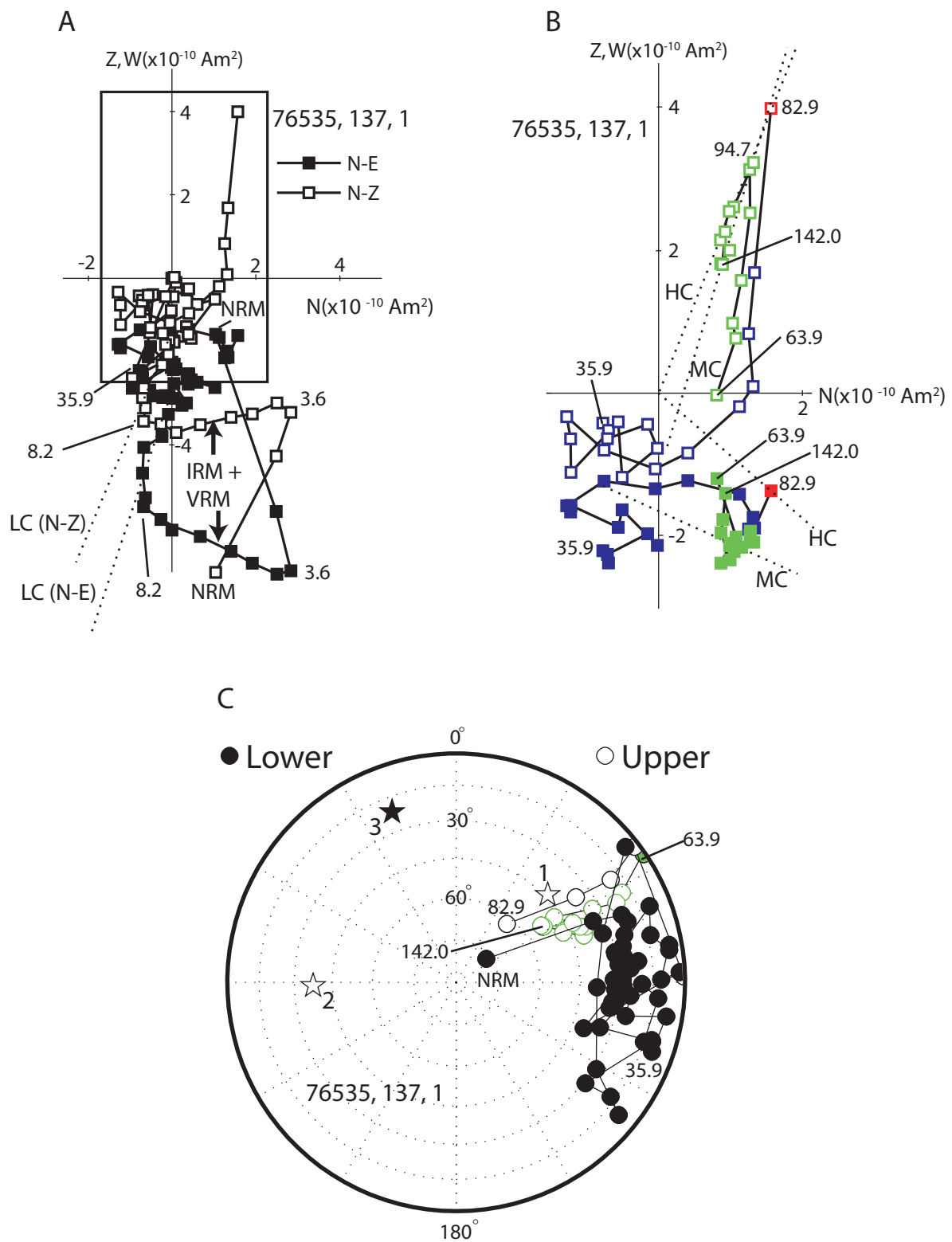
function of DC bias field. Lower dotted curve is that of highly interacting chiton tooth magnetite and upper dotted curve is noninteracting magnetite in magnetotactic bacteria. (A) 76535,137,3. (B) 76535,137,5.

**Fig. S9.** Isothermal remanent magnetization (IRM) acquisition and demagnetization experiments on selected subsamples of 76535.  $f_{IRM}$  = fraction of IRM remaining/lost. (A) IRM acquisition and alternating field (AF) demagnetization of IRM by 76535,137,3. Both curves are normalized to the highest-field IRM value. (B) Derivative of IRM acquisition (purple crosses) and AF demagnetization of IRM (light blue crosses), with running average given by solid lines. (C) IRM acquisition and AF of IRM for 76535,137,5. (D) Derivatives of IRM acquisition and AF of IRM for 76535,137,5.

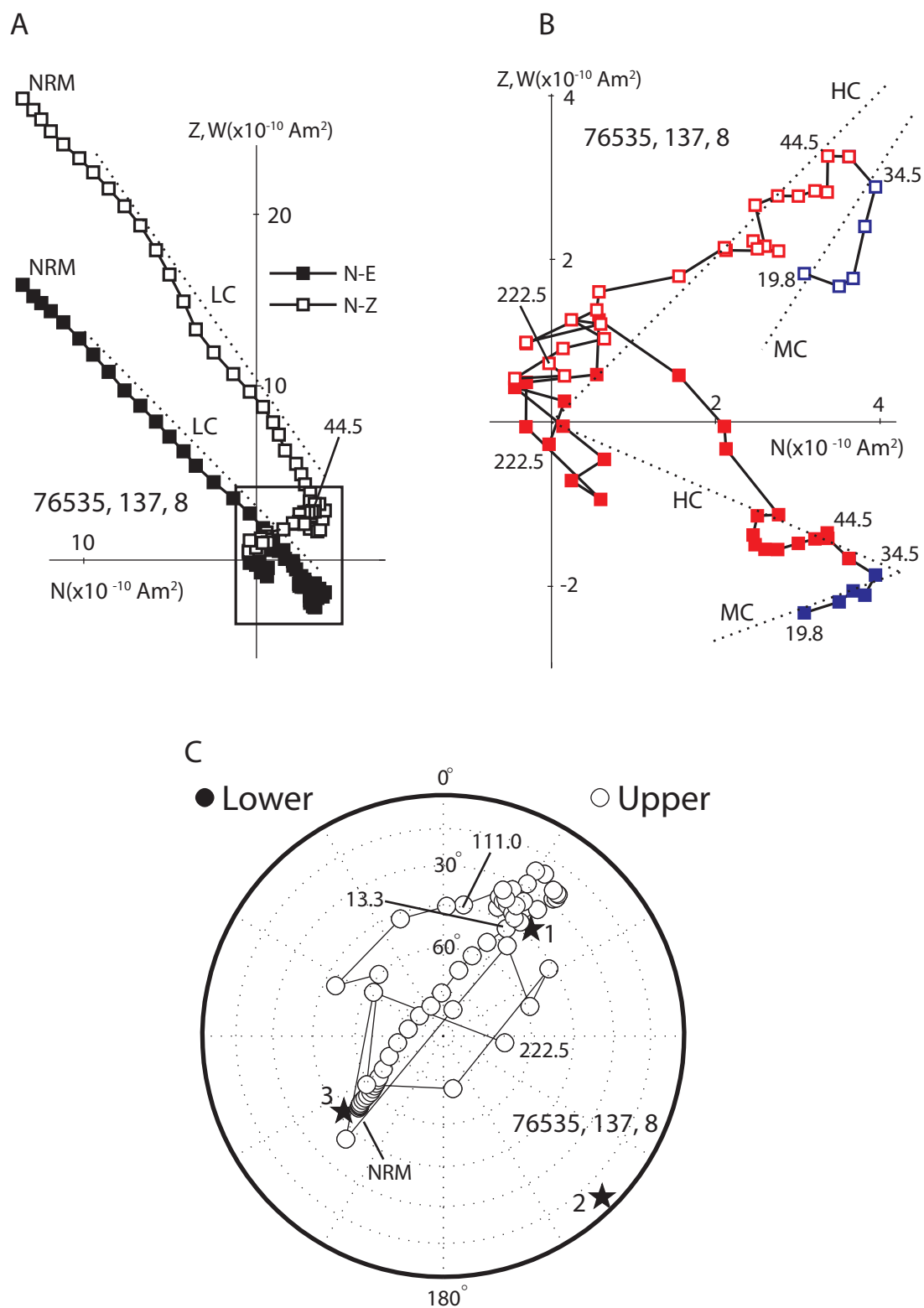
**Fig. S10.** Lowrie-Fuller tests for selected subsamples of 76535. Shown is alternating field demagnetization of an anhysteretic remanent magnetization (ARM) acquired in a 200 mT peak AC field with 0.2 mT DC bias field (light blue symbols) and of an isothermal remanent magnetization (IRM) acquired in a 200 mT field. Both curves are normalized to the starting value just prior to AF demagnetization. (A) 76535,137,3. (B) 76535,137,5.

**Fig. S11.** Room temperature hysteresis loops for 76535. Shown is the sample moment as a function of applied field. Inset shows data near origin (between -60 and 60 mT). (A) 76535,137,1. (B) 76535,137,3.

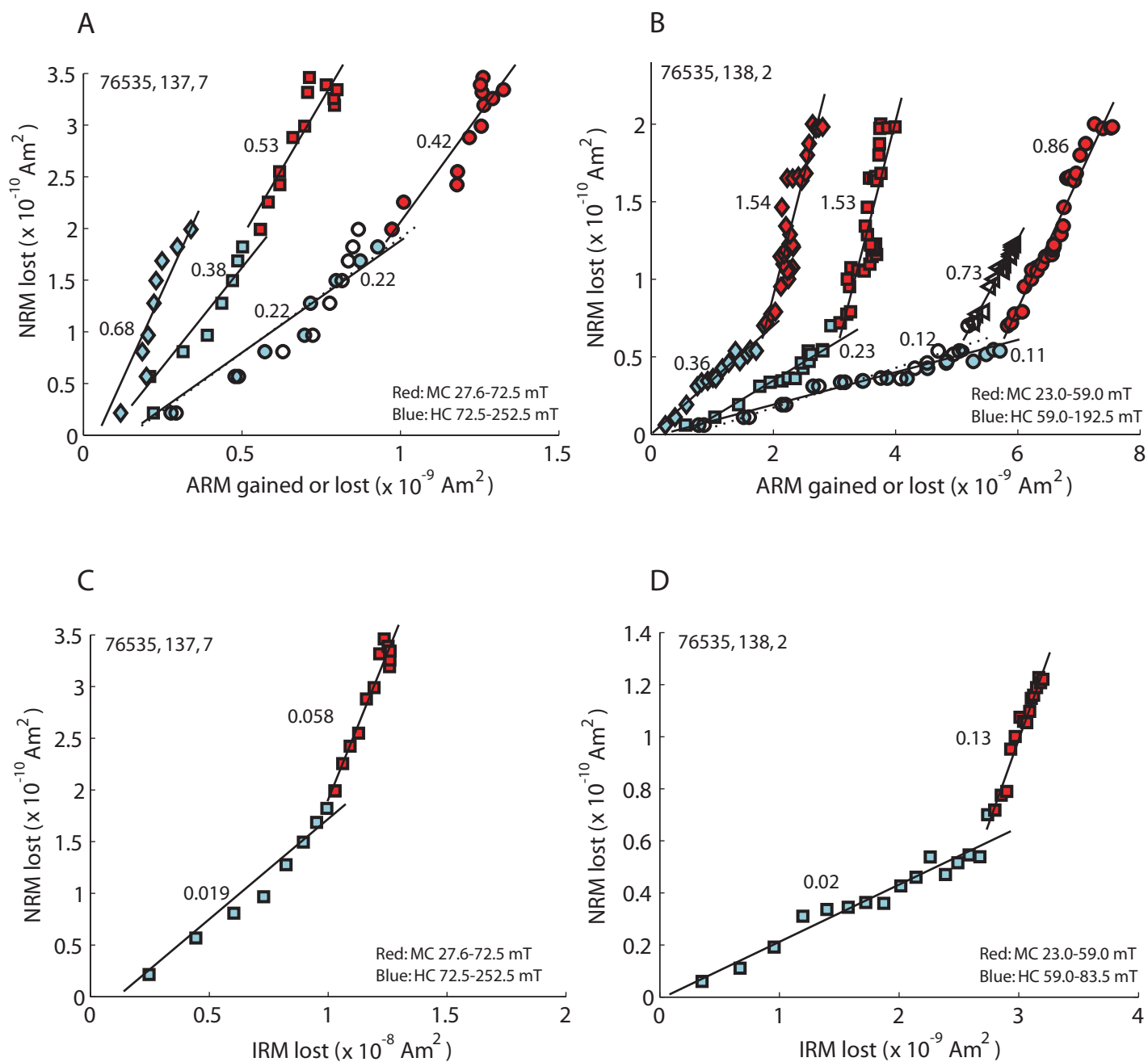
**Fig. S12.** Diffusive heating and cooling calculations for masses of lunar rock. (A) Black curves give the temperature of a spherical rock of radius  $R$  at a radius  $r = R/2$ , with initial temperature  $T_0 = -20^\circ\text{C}$ , surrounded by a medium of  $T_0 = 770^\circ\text{C}$ . Curves are calculated for four values of  $R$  (2.5 cm, 25 cm, 2.5 m, and 25 m). (B) Red curves give the temperature of a spherical rock (or ejecta blanket) of radius  $R$  at a radius  $r = R/2$ , with initial temperature  $T_0 = 770^\circ\text{C}$  surrounded by a medium of  $T = -20^\circ\text{C}$ . Curves are calculated for four values of  $R$  (2.5 cm, 25 cm, 2.5 m, and 25 m).



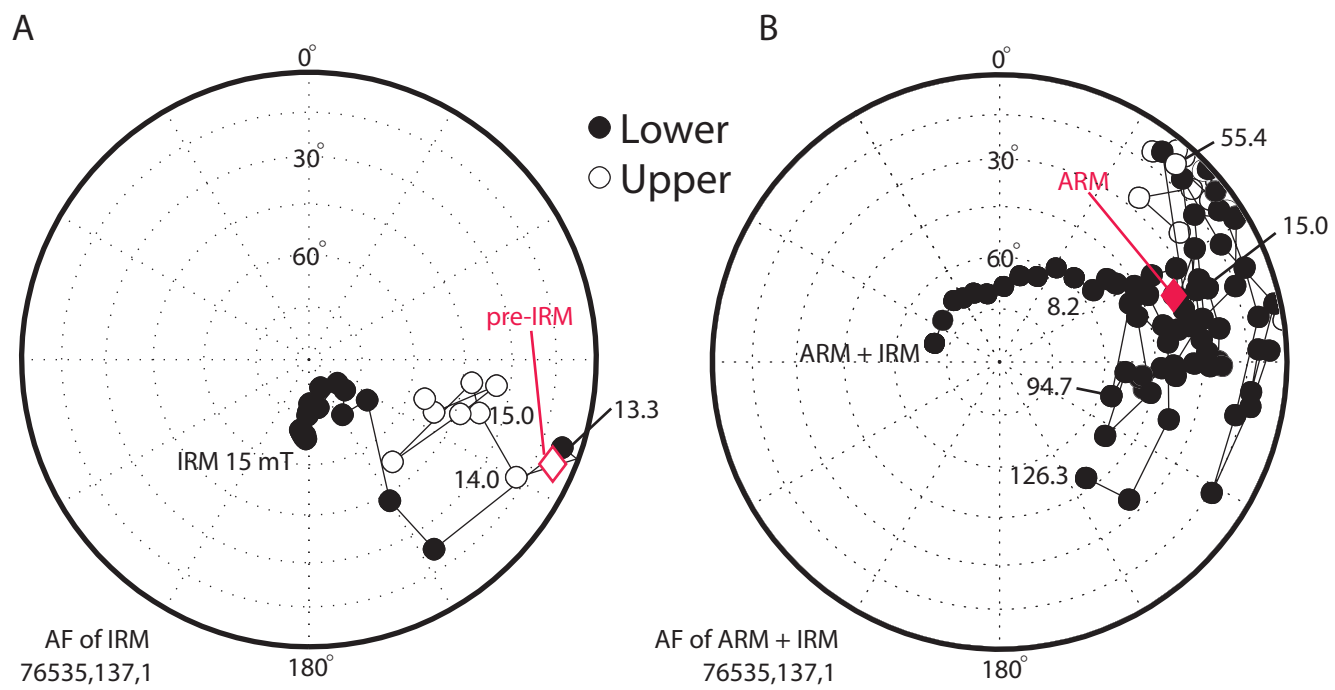
Garrick-Bethell et al. Figure S1



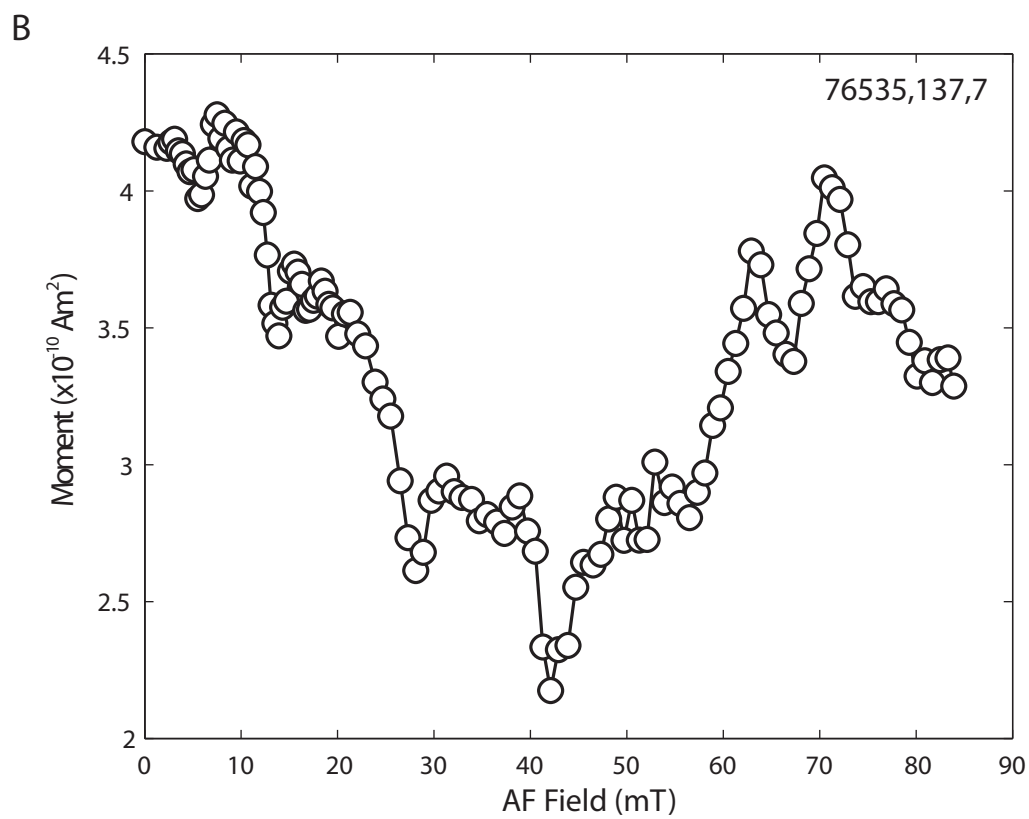
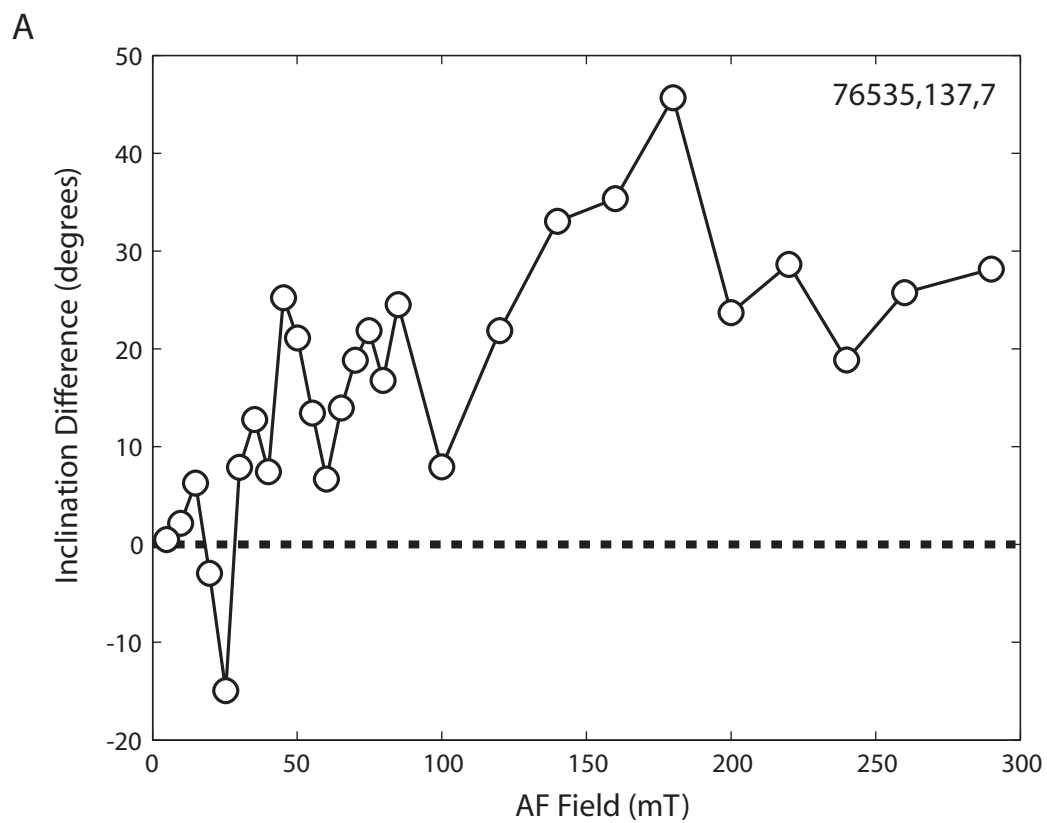
Garrick-Bethell et al. Figure S2

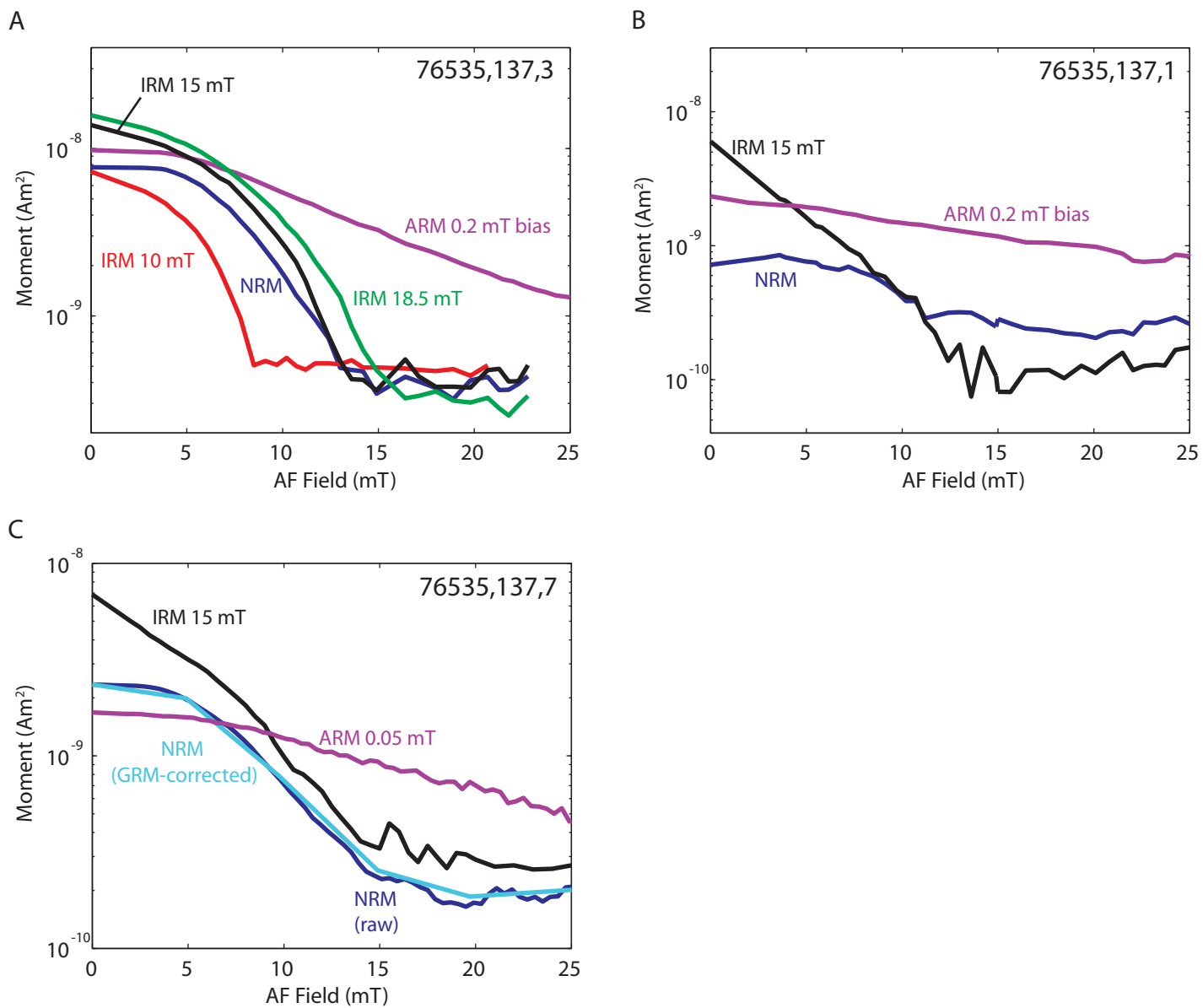


Garrick-Bethell et al. Figure S3



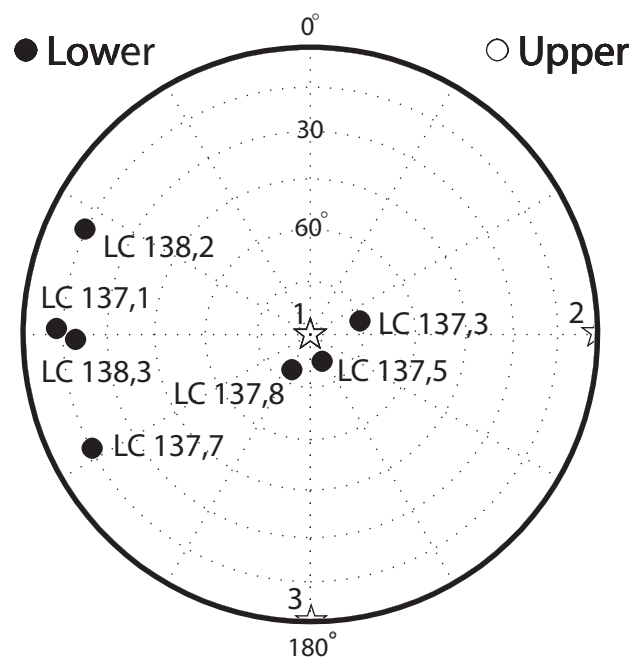
Garrick-Bethell et al. Figure S4





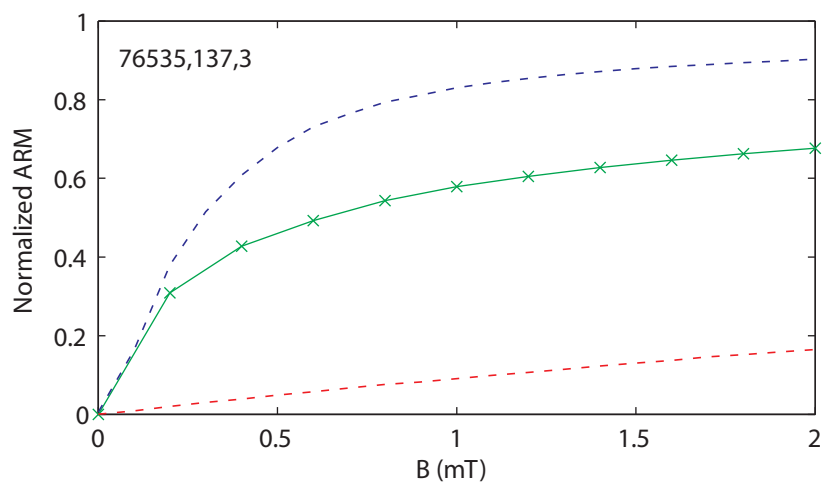
Garrick-Bethell et al. Figure S6



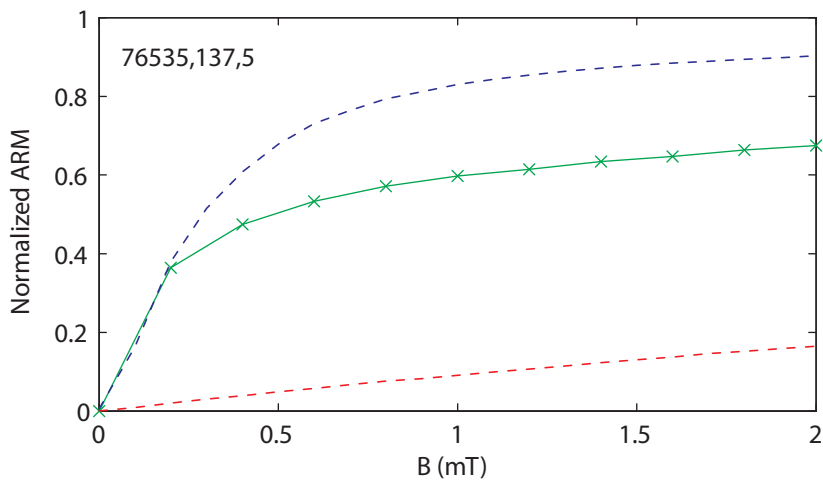


Garrick-Bethell et al. Figure S7

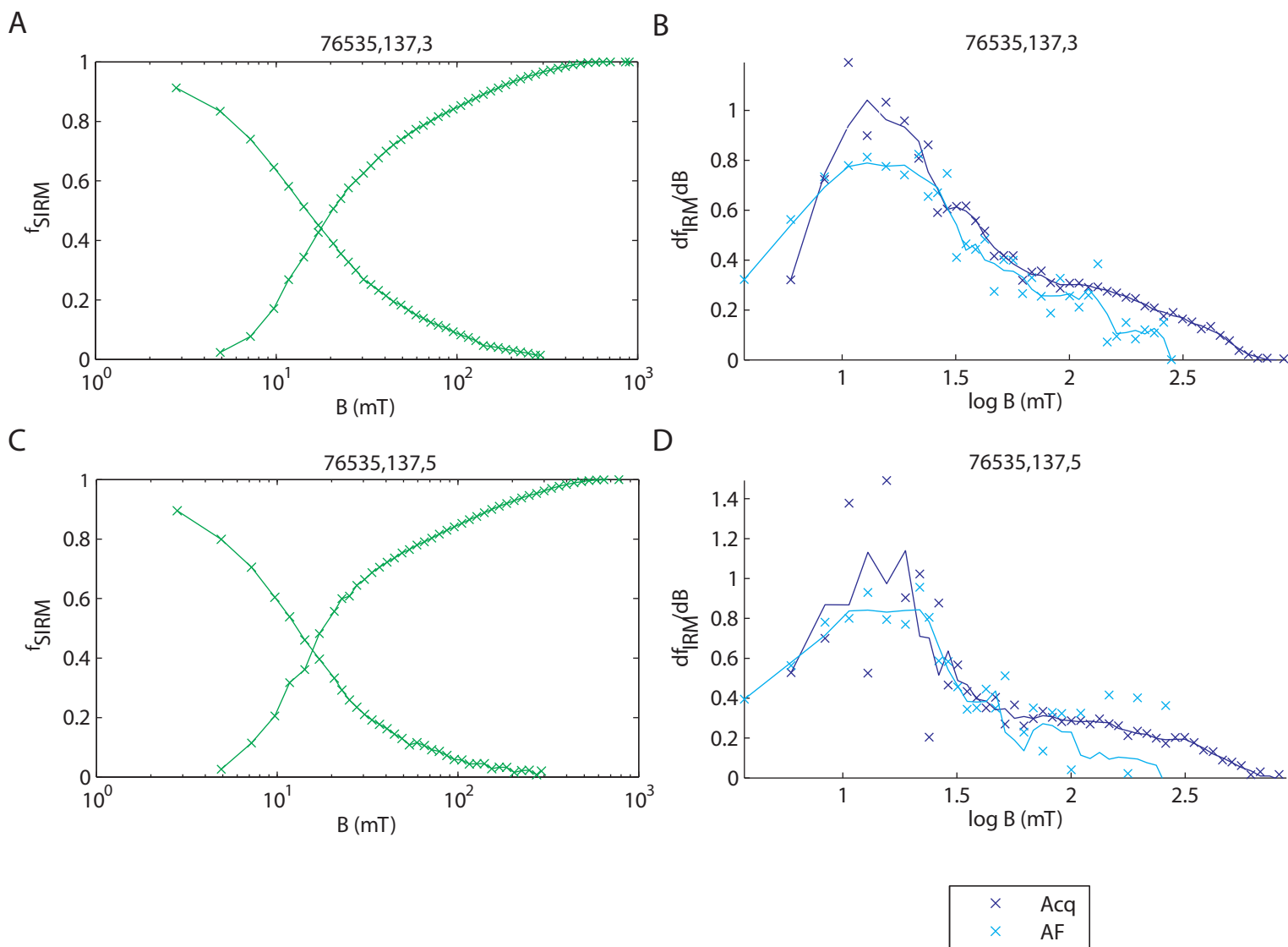
A



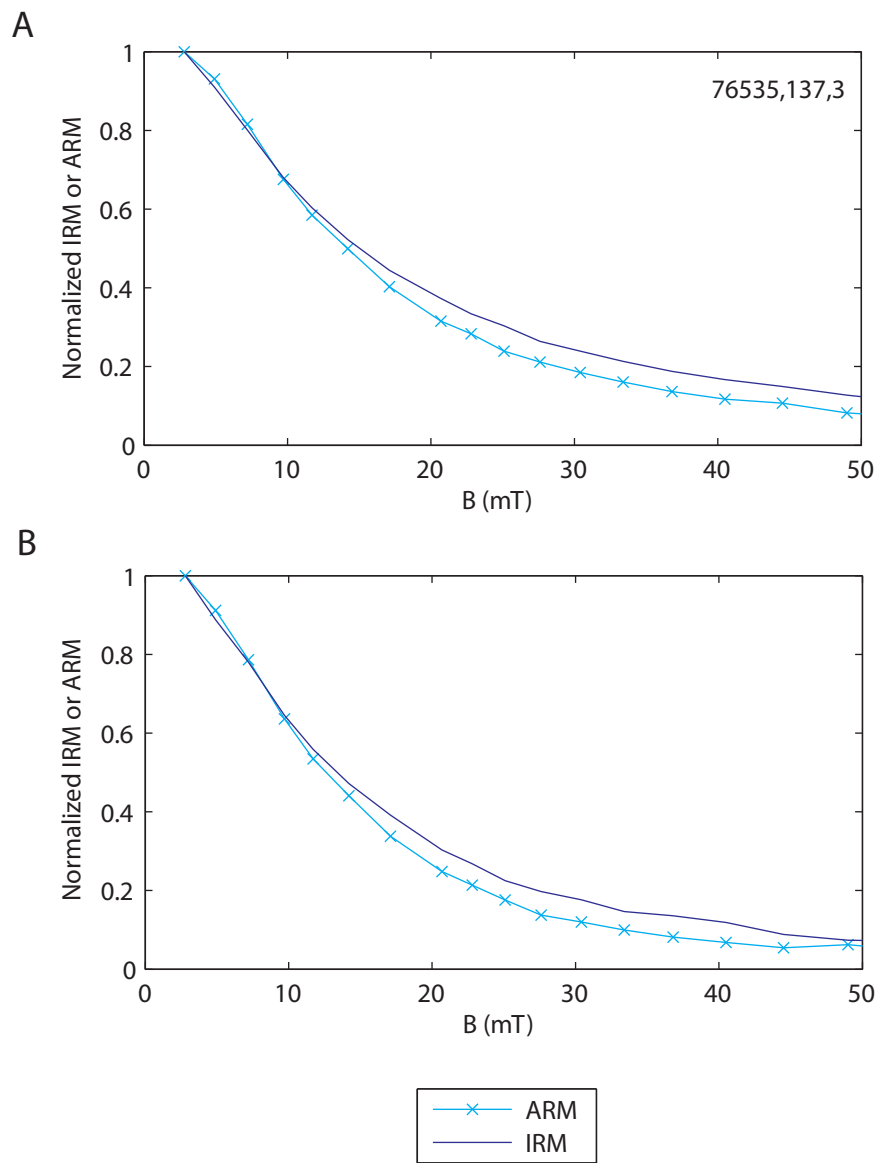
B



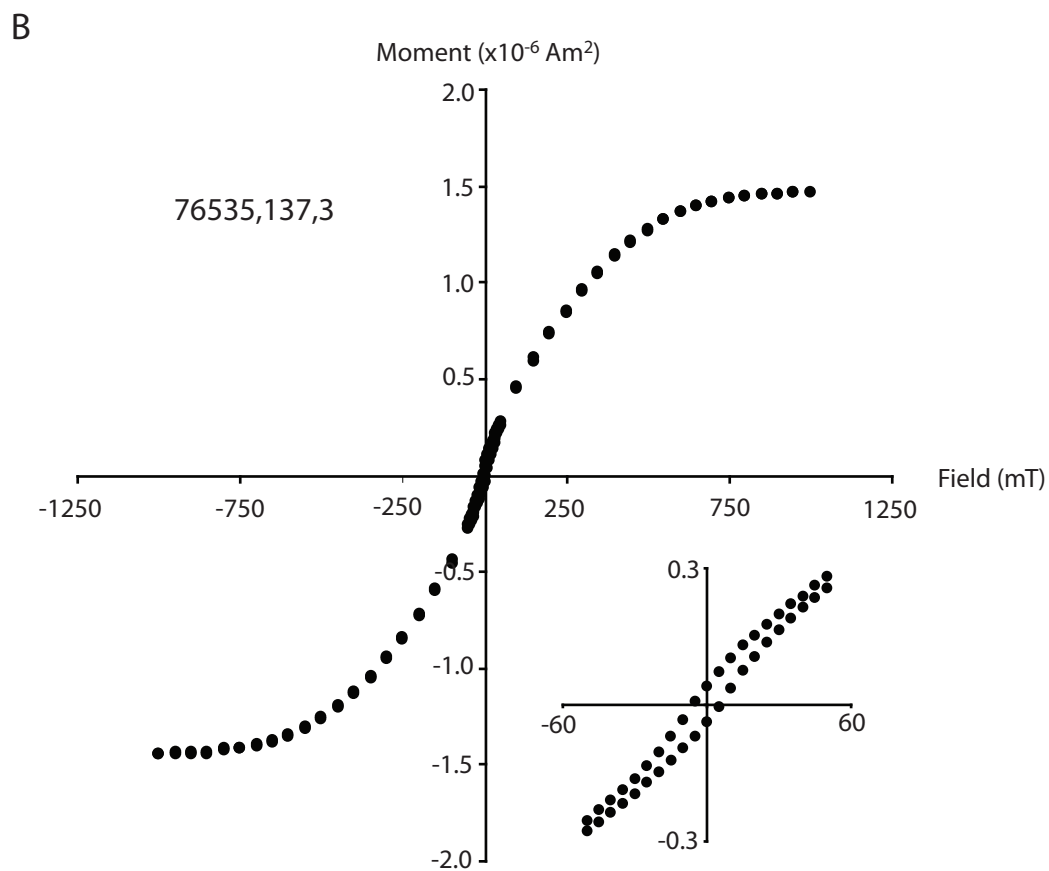
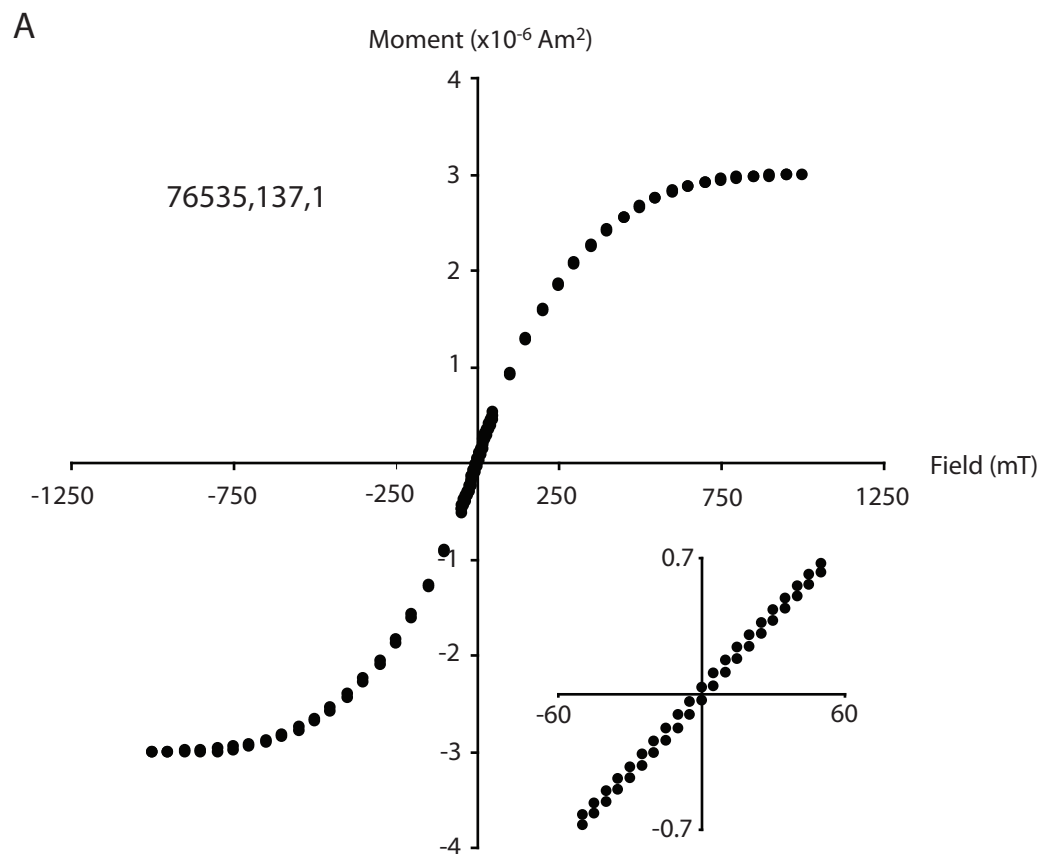
Garrick-Bethell et al. Figure S8

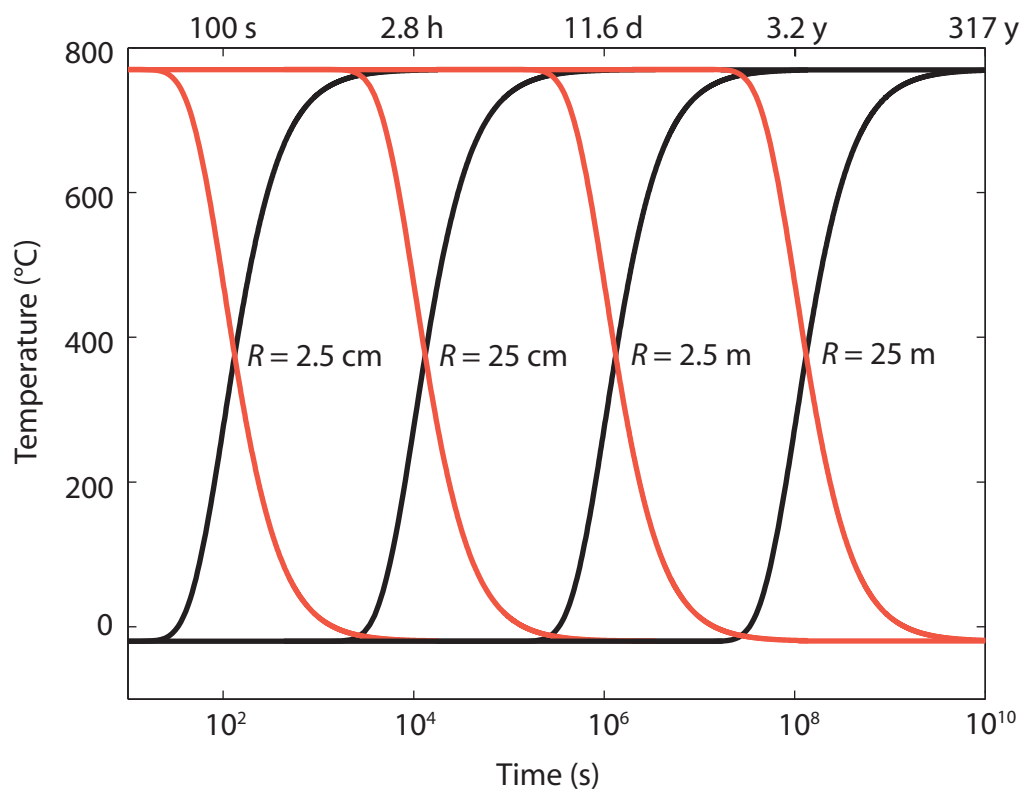


Garrick-Bethell et al. Figure S9



Garrick-Bethell et al. Figure S10





Garrick-Bethell et al. Figure S12